Check for updates

Earthquake Engineering & Structural Dynamics

WILEY

RESEARCH ARTICLE OPEN ACCESS

Seismic Capacity and Performance of Waffle-Flat Plate Structures Under Near-Fault Ground Motions: Bidirectional Shake Table Tests

Amadeo Benavent-Climent[1] | David Galé-Lamuela[1] | Jesús Donaire-Avila[2]

[1]Department of Mechanical Engineering, Universidad Politécnica de Madrid, Madrid, Spain | [2]Department of Mechanical and Mining Engineering, University of Jaen, Jaén, Spain

Correspondence: Amadeo Benavent-Climent (amadeo.benavent@upm.es)

Received: 24 February 2025 | **Revised:** 14 May 2025 | **Accepted:** 20 June 2025

Funding: This work was supported by the Spanish Ministry of Science MCIN/AEI/10.13039/501100011033/[PID2023-152739OB-I00]; and FEDER (Fonds Européen de Dévelopment Régional).

Keywords: bidirectional response | energy dissipation | near-fault ground motions | shake table test | waffle-flat plate

ABSTRACT

A reinforced concrete waffle-flat plate structure was subjected to a sequence of bidirectional near-fault ground motions on a shake table until collapse. The test specimen was designed under current building codes and assigned a region of moderate seismicity. The ground motions were scaled in amplitude to represent very frequent, frequent, design, and very rare earthquakes at the site. Under these levels of seismic action the structure did not exceed the limit states established by the second generation (2G) of Eurocode 8, although collapse occurred under a seismic action slightly less severe than expected due to the accumulation of damage caused by previous tests. A large amount of energy was dissipated through torsion of the transverse beams by means of a brittle internal mechanism that was not intended to occur. Damage concentrated at the exterior plate-to-column connection (torsion failure of the transverse beams), which dissipated 63% of the total input energy and 93% of the energy that contributes to damage (i.e., input energy minus energy dissipated by inherent damping). In comparison with the plate, the columns dissipated a very small amount of energy (less than 7%). The total energy input on the structure until collapse under near-fault bidirectional seismic actions was close to that obtained in previous studies with a similar specimen under unidirectional or under bidirectional far-field ground motions. Finally, the behavior factor obtained from the capacity curve —estimated using the experimental base shear vs. top displacement relationship (1.55) — was very close to the behavior factor ($q = 1.6$) prescribed by the 2G of Eurocode 8 for torsionally flexible WFP systems for use in force-based seismic design methods.

1 | Introduction and Research Significance

Structures consisting of reinforced concrete (RC) flat plates (FP), whether solid or waffle (WFP), directly supported on columns, have advantages over the frame systems for supporting gravity loads: they are more cost-effective, provide more freedom for locating columns and the layout of partitions in plan, can cover larger spans with smaller depths, increase the clear story height, and do not obstruct conduits or piping placed under the ceiling. Their main drawbacks can arise when used for resisting lateral seismic loads because they have low horizontal stiffness. For these reasons, and because very few present-day codes include provisions for their seismic design, FP or WFP systems are not common in new construction in regions of moderate or high

This is an open access article under the terms of the Creative Commons Attribution-NonCommercial-NoDerivs License, which permits use and distribution in any medium, provided the original work is properly cited, the use is non-commercial and no modifications or adaptations are made.

© 2025 The Author(s). *Earthquake Engineering & Structural Dynamics* published by John Wiley & Sons Ltd.

seismicity. The current Eurocode 8, EN1998-1 [1] does not cover this type of system as a seismic-action-resisting system of the Ductility Class (DC) medium (M) or high (H); EN 1998-1 simply states that FP systems may be designed for DC low (L) with a behavior factor $q \leq 1.5$, and should be used only for low seismicity regions. The second generation (2G) Eurocode 8 [2] will cover RC FP systems, but limiting its ductility class to the new DC2—that is, in between the DCL and the DCM of current Eurocode 8—and only for very low to moderate seismic action classes. The current Spanish Seismic code NCSE-02 [3] limits the behavior factor μ (counterpart of factor q in EN 1998-1) to $\mu = 2$. Neither EN 1998-1 nor NCSE-02 provide dimensioning and detailing rules for FP or WFP systems. This lack of coverage in codes is mostly due to an insufficient accumulation of knowledge concerning seismic performance.

Past experimental research has focused on solid slab-column connections (most of them internal joints) to show the effects of column size, slab thickness, amount and layout of longitudinal reinforcement, use of transverse reinforcement, or the loading protocol on the resistance to punching shear and on the rotation capacity and ductility of the connections. Robertson and Johnson [4] investigated the seismic response of nonductile slab-column connections with discontinuous reinforcement through cyclic lateral loading, concluding that punching shear failure does not appear to occur earlier than in the equivalent specimens with continuous reinforcement, but the consequences are more severe. Drakatos et al. [5] tested 13 full-scale internal FP-column connections and showed that cyclic loading led to significant moment strength and deformation capacity reduction when compared to results obtained from monotonic loading tests; these effects of cyclic loading were more pronounced for slabs with low reinforcement content. A review of tests on solid FP-column connections conducted by Zhou and Hueste [6] and Ramos et al. [7] likewise showed that larger gravity shear ratios (defined here as ratio between the acting vertical shear force and the punching shear resistance) imply lower horizontal deformation capability, and that the horizontal drift capacity is significantly increased when shear reinforcement is used.

Although to a lesser extent, tests have also been carried out on FP floors and FP multistory structures. Most are quasi-static tests. Rha et al. [8] tested five two-bay continuous FP floors under monotonic and cyclic static loads and found a significant influence of the loading protocol. Under monotonic loading, the reduction of the load after reaching the maximum load and before all connections reached failure was minor. Under cyclic loading, however, a sizeable reduction of the lateral force occurred after the first punching failure of the internal slab-column connection. Fick et al. [9] studied a full-scale three-story, two-bay RC FP structure designed to resist gravity loading, which was tested to failure under cycles of quasi-static imposed lateral displacements. They found that the structure suffered very limited damage until a drift ratio of 1.5%, whereas at a roof drift ratio of 2.9% one of the internal slab-column connections reached failure due to punching at a story drift ratio level of 3.3%. More recently, a real-scale building with FP systems was tested for seismic and cyclic loading with the reaction wall facility of the Joint Research Center in the ELSA laboratory [10]. These tests confirmed the reports in the literature, mainly based on isolated connections and/or small-scale samples. Dynamic tests using shake tables are very scarce. Kang and Vallace [11] tested a two-story one-bay FP structure under unidirectional shake table tests and found substantially less drift capacity than when testing isolated connections. Benavent-Climent et al. [12] tested a WFP structure designed following modern codes under one horizontal component of a far-field ground motion on a shake table and evaluated its seismic performance. Based on the test results, the authors proposed a (force reduction) behavior factor of $q = 3$ for designing this type of system using force-based methods. The effects of the bidirectional seismic action were also investigated by Benavent-Climent et al. [13] by testing a WFP structure under two horizontal components of a far-field ground motion on a bidirectional shake table, and consequently proposing to reduce the factor to $q = 2$. A complete state-of-the-art on FP floors and multistory structures can be found in Coronelli et al. [14].

The lack of coverage of FP systems in codes may give the impression that they are not appropriate in seismic zones. Yet this is not necessarily true. Although our knowledge about this type of system needs to be extended, some experimental evidence indicates that FP structures can exhibit ductility and energy dissipation capacity large enough to satisfy the demands of structures located in moderate or even high seismicity regions, provided that: (i) they are protected from punching failure; (ii) the potential of damage concentration in a single (or a few) stories is controlled; and (iii) the lateral displacements are limited to control second-order (P-delta) effects and drift-induced damage on the auxiliary elements. Fardis [15] highlights the need to further investigate FP systems so that "the cost-effectiveness and seismic performance of earthquake resistant concrete buildings will benefit from the rational use of flat slab frames as part of the lateral-load-resisting system." Required investigations include addressing the performance of FP or WFP systems under highly demanding seismic scenarios such as near-fault ground motions, and up to collapse. Near-fault ground motions impose on structures large demands compared to far-field ground motions [16]. In the proximity of a fault, ground motions are significantly affected by forward directivity as well as possible static deformation of the ground surface associated with fling-step effects. Such near-fault outcomes cause most of the seismic energy to arrive at the structure in a few long-period velocity pulses that forces the structure to dissipate the input energy through few large excursions of plastic deformation [17]. Past studies [18] showed that pulses increase not only the peak inelastic displacements, but also —and almost proportionally— the residual displacements. Peak and residual displacements are especially critical in inherently flexible structures such as FP systems. Additional research is also needed on the response under bidirectional cyclic loadings, which is known to be critical in the performance of FP systems. The optimal source for experimental information to capture the influence of these effects is the bidirectional (or multidirectional) dynamic shake table test. It can reproduce in the most realistic way the complex response of RC elements under severe seismic loadings, and can capture rate-of-loading effects such as the variation of mechanical properties of materials. To the authors' knowledge, there are no documented bidirectional shake table tests of overall or partial WFP structures subjected to near-fault ground motions. The present study tries to fill this gap by assessing, through bidirectional shake table testing, the seismic capacity and performance of WFP systems designed following current seismic codes under near-fault ground motions.

10969845, 0, Downloaded from https://onlinelibrary.wiley.com/doi/10.1002/eqe.70016 by Readcube (Labtiva Inc.), Wiley Online Library on [01/07/2025]. See the Terms and Conditions (https://onlinelibrary.wiley.com/terms-and-conditions) on Wiley Online Library for rules of use; OA articles are governed by the applicable Creative Commons License

2 | Prototype Structure and Test Specimen

2.1 | Prototype Structure

Figure 1 shows the prototype structure from which the test specimen was defined. It consists of a three-story RC WFP system supported on isolated columns. It was designed applying the Spanish concrete code EHE-08 [19] to sustain gravity loads and lateral seismic loads established under the current Spanish Seismic Code NCSE-02. The dead and live loads considered were 3.13 and 2 kN/m^2 respectively for floors; and 3.46 and 1 kN/m^2 for the roof. The building was categorized as consequence class CC2 (residential) and it was assumed to be in Granada (Spain) on soil type C ($180 < v_{s,30} < 360$; here $v_{s,30}$ is the average shear wave velocity in m/s). Figure 2a shows with bold solid lines the (unscaled) 5% damped acceleration spectrum that characterizes the seismic hazard used in design; it corresponds to a return period of 475 years. The seismic design was undertaken using force-based methods with the maximum behavior factor allowed by NCSE-02 for WFP systems ($\mu = 2$). The mechanical properties assumed for the materials were: $f_c = 25$ MPa for the characteristic cylinder concrete compressive strength and $f_y = 500$ MPa for the characteristic tensile yield strength of steel. The design did not consider reinforcement details nor capacity criteria to guarantee a strong column-weak plate plastic mechanism under lateral loads. Therefore, the results from the experiments conducted in this study are applicable (limited) to low ductility waffle-flat plate RC buildings that can develop a column-sway plastic mechanism under lateral loads. Notwithstanding, the solid zones around the columns were dimensioned and reinforced to avoid punching failure. Capacity design and ductile detailing were used for the columns so that flexure failure would precede shear failure. The resulting prototype structure consisted of plates having 0.35 m depth with a regular pattern of voids and a solid zone around the columns. The voids formed an orthogonal grid of ribs spaced 0.83 m. The plate was surrounded by transverse beams of the same depth. The resulting design base shear force coefficient was $\alpha_{design} = 0.33$.

2.2 | Test Specimen

The partial structural model shown in Figure 1 with the hatched area was separated from the prototype. The height of the partial structural model is one story and a half. There is no continuity of the plate beyond the internal supports, and this may alter the state of stress and deformation over the supporting columns. However, the purpose of the experiments was to investigate the behavior of the test specimen under earthquake-type dynamic loading, not to reproduce the particular response that the partial structural model would experience inside the overall three-story prototype. The latter is influenced by dynamic interactions with the other parts of the structure. Therefore, the results of the test specimen cannot be extrapolated to the response of the

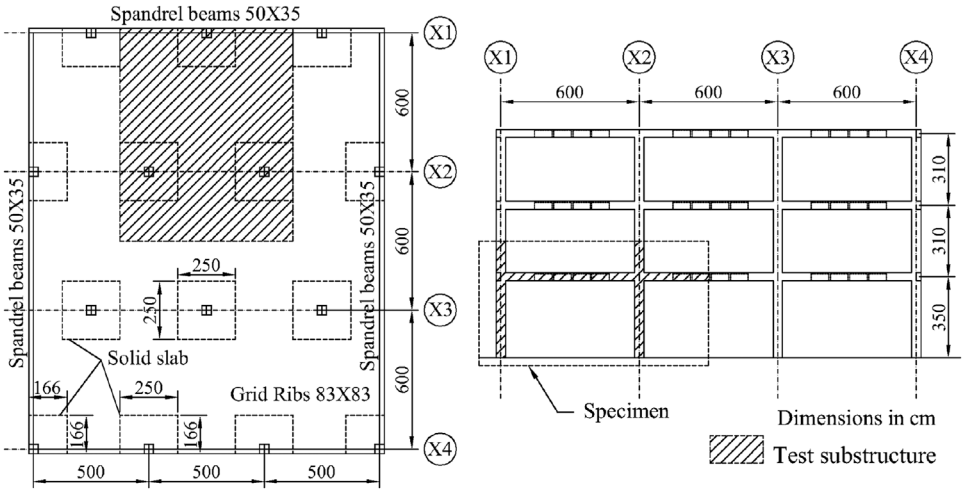

FIGURE 1 | Prototype structure: plan (left); elevation (right). Units in centimeters.

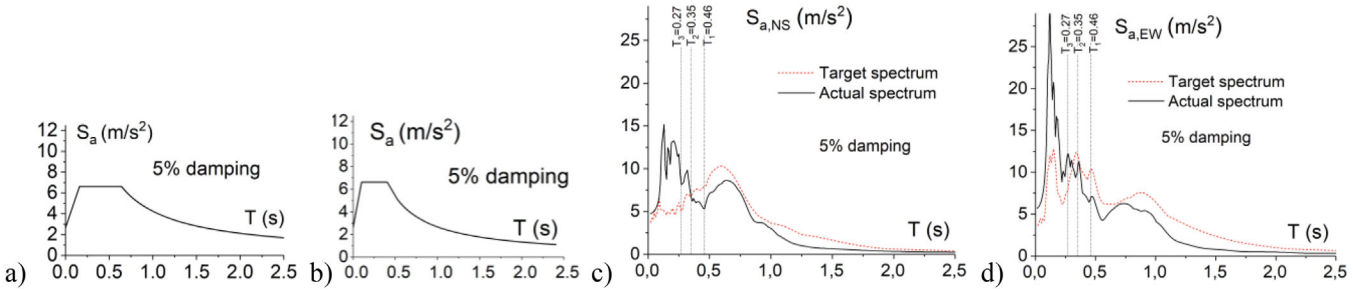

FIGURE 2 | (a) elastic spectrum used for design unscaled in time; (b) elastic spectrum used for design scaled in time by 0.63; target and actual spectra of the NS (c) and EW (d) components of test B_{475}.

10969845, 0, Downloaded from https://onlinelibrary.wiley.com/doi/10.1002/eqe.70016 by Readcube (Labtiva Inc.), Wiley Online Library on [01/07/2025]. See the Terms and Conditions (https://onlinelibrary.wiley.com/terms-and-conditions) on Wiley Online Library for rules of use; OA articles are governed by the applicable Creative Commons License

3-story prototype. The dimensions and characteristics of the test specimen were determined from a partial structural model by applying scale factors of $\lambda_L = 2/5$ for length, $\lambda_a = 1$ for acceleration, and $\lambda_\sigma = 1$ for stress. Similitude requirements were applied to scale the rest of the physical quantities, giving a scaling factor of $(2/5)^{0.5} = 0.63$ for time. The design spectrum scaled in time by 0.63 is shown in Figure 2b. Figure 3 shows the resulting test specimen. The full-scale prototype structure used ribbed bars of diameters 20 and 16 mm as longitudinal reinforcement, whose cross-section areas are $A_{20} = 314.2$ mm^2 and $A_{16} = 210.1$ mm^2, respectively. In the scaled test specimen these bars were represented by ribbed bars of diameter 8 and 6 mm, respectively, whose cross-section areas $A_8 = 50.3$ mm^2 and $A_6 = 28.3$ mm^2, are very close to the target scaled values, i.e. $(2/5)^2 \times 314.2 = 50.3$ mm^2 and $(2/5)^2 \times 210.1 = 33.6$ mm^2, respectively. The full-scale structure also used ribbed bars of diameter 10 mm as stirrups having an area of $A_{10} = 78.5$ mm^2. They were represented in the test specimen by ribbed steel wires of diameter 4 mm whose area $A_4 = 12.6$ mm^2 coincides with the target scaled value $(2/5)^2 \times 78.5 = 12.6$ mm^2. This study focused on new structures designed according to current seismic codes that include requirements to prevent the anchorage failure of the reinforcement. Accordingly, the development lengths of the bars in the test specimen were designed to prevent anchorage failure, considering the actual surface conditions (ribs) and the actual yield stress of the steel. The yield stress of the longitudinal rebars of diameter 8 mm (Ø8) and 6 mm (Ø6) amounted to 525 and 543 MPa. The yield stress of the steel used for the stirrups was 656 MPa. The Ø4 steel wire was not treated (annealed) to match its properties (yield stress) to that of the prototype. The compression strengths of the concrete were 43 MPa on the 28th day, and 44 MPa on the day of the tests. These strengths are higher than the ones assumed in the design, most probably due to the chemical admixtures used to make the concrete more fluid and facilitate casting. The concrete overstrength was not considered in the design of the prototype, though it was considered when processing the results of the tests. The yield moment of the column sections and of the solid zones of the plate around the columns was not affected by the concrete compressive strength. Therefore, the hierarchy of flexural strength between columns and plate was not altered by the increment of concrete compressive strength, and thus it can be considered that the plastic mechanisms in the test represented the plastic mechanisms expected in the full-scale structure. The ratios of longitudinal reinforcement area A_{sl} to gross section area A_g were: $A_{sl}/A_g = 0.031$ and $A_{sl}/A_g = 0.024$ for the exterior and interior columns, respectively, of the first floor; and $A_{sl}/A_g = 0.018$ for the columns of the second floor. The volumetric ratio of the shear reinforcement $\rho_{st} = V_{st}/V_{cc}$ was 0.03 for interior columns of the first floor, and 0.02 for the rest. Here $V_{st} = nA_{st}l_s$ is the volume of the shear reinforcement (n, A_{st}, l_s are the number, cross-section area, and length of the stirrups) and V_{cc} denotes the volume of concrete confined by the shear reinforcement. The WFP had an upper and lower base reinforcement consisting of a mesh of Ø6 bars spaced 332 mm. Additional Ø6 mm and Ø8 mm longitudinal bars were located on the solid zone of the plate around each column (see Figure 3b,c). The specimen is torsionally flexible according to the criterion established by 2G of Eurocode 8—i.e., the minimum torsional radius divided by the radius of gyration of the floors is less than one.

3 | Description of the Tests

3.1 | Test Setup and Instrumentation

The specimen was tested at the Laboratory of Structural Dynamics of the University of Granada (Spain) with a bidirectional MTS 3 × 3 m^2 shake table. Figure 4 shows the test setup and the instrumentation. Figure 5 offers a general view. Steel blocks were attached at the top of the plate and at the top half of columns of the second story to represent the gravity loads acting on the floors and to satisfy similitude requirements. The effect of the moments expected in the full-scale structure along the continuous spans is considered along the X direction by extending the plate beyond the columns and connecting the edge of the RC plate with the steel plates put on the top of the specimen by means of pin-ended steel bars (see Figure 4a). The steel plates have very large flexural stiffness in comparison with that of the RC plate and the axial stiffness of the pin-ended steel bars is also very large. The specimen was instrumented with accelerometers, displacement transducers (LVDTs and lasers), and 472 strain gauges. Gauges were fixed to the longitudinal reinforcement at the ends of the columns at sections of potential plastic hinges; they are identified in Figure 4a with solid circles labeled S10, S11, and S12 for column C1; S20, S21, and S22 for column C2; and S30, S31, and S32 for column C3. Gauges were fixed to the longitudinal reinforcement of the solid parts of the plate around the exterior column C1 and around the interior column C3, at the positions indicated with solid circles in Figure 4b. The critical sections on the solid parts of the plate around the columns are labeled with a name beginning in S and ending in the name of the axis along which the gauges measure the strains. Gauges were moreover fixed to the longitudinal reinforcement of the transverse (edge) beams in the vicinity of column C1, and at the critical sections named S8Y and S9Y in Figure 4b. Four compression-only load cells were installed at the top end of each column of the second story to measure the forces transferred by the inertial masses in two orthogonal horizontal directions. The displacement transducers (LVDTs and lasers) shown in Figure 4c,d served to measure in-plane translations and interstory drifts (IDs). The scanning frequency of the data acquisition system was 600 Hz. The data acquisition system continued measuring from the instant t_o at which the shake table stopped, until the instant t_{end} at which the test specimen completely ceased its movement. Several video cameras recorded the tests.

3.2 | Tests

The specimen was subjected to seven consecutive tests. In each, the NS and EW acceleration components of the near-fault ground motion recorded at Bar-Skupstina Opstine (magnitude $M_w = 6.9$, epicentral distance 16 km, fault distance 12 km), scaled in time by factor $\lambda_t = (\lambda_L/\lambda_a)^{0.5} = 0.63$, were applied simultaneously. The NS component was applied in the direction X of the specimen (see Figure 3), and the component EW in the perpendicular direction Y. In the tests, the acceleration of the recorded ground motion was scaled in amplitude to increasing values up to the collapse of the specimen. Figure 2c,d shows the 5% damped spectra of the Bar-Skupstina Opstine ground motion scaled in time by 0.63 and scaled in amplitude to represent the design basis earthquake

10969845, 0, Downloaded from https://onlinelibrary.wiley.com/doi/10.1002/eqe.70016 by Readcube (Labtiva Inc.), Wiley Online Library on [01/07/2025]. See the Terms and Conditions (https://onlinelibrary.wiley.com/terms-and-conditions) on Wiley Online Library for rules of use; OA articles are governed by the applicable Creative Commons License

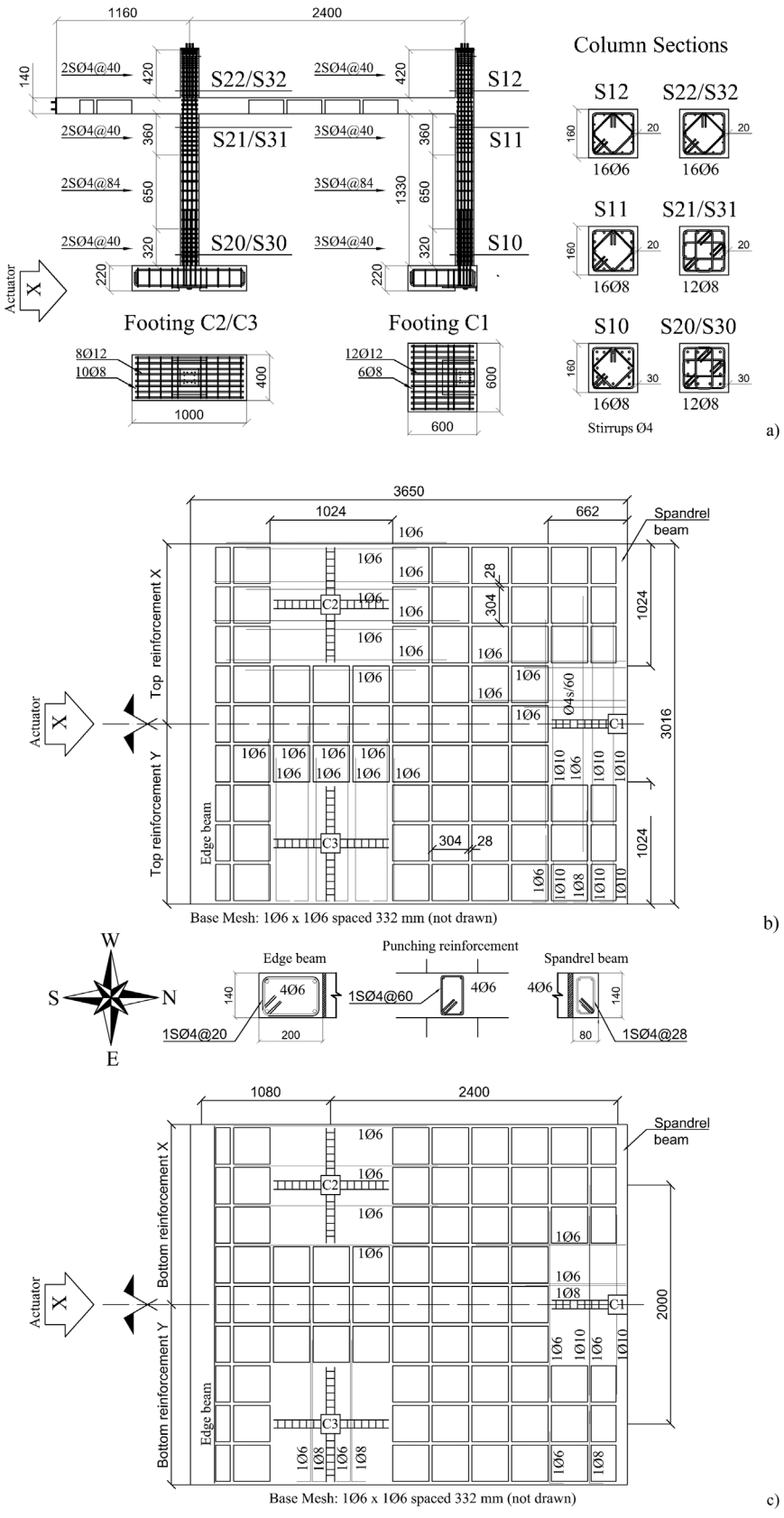

FIGURE 3 | Test specimen (dimensions in mm): (a) elevation, (b) top, and (c) bottom reinforcement.

10969845, 0, Downloaded from https://onlinelibrary.wiley.com/doi/10.1002/eqe.70016 by Readcube (Labtiva Inc.), Wiley Online Library on [01/07/2025]. See the Terms and Conditions (https://onlinelibrary.wiley.com/terms-and-conditions) on Wiley Online Library for rules of use; OA articles are governed by the applicable Creative Commons License

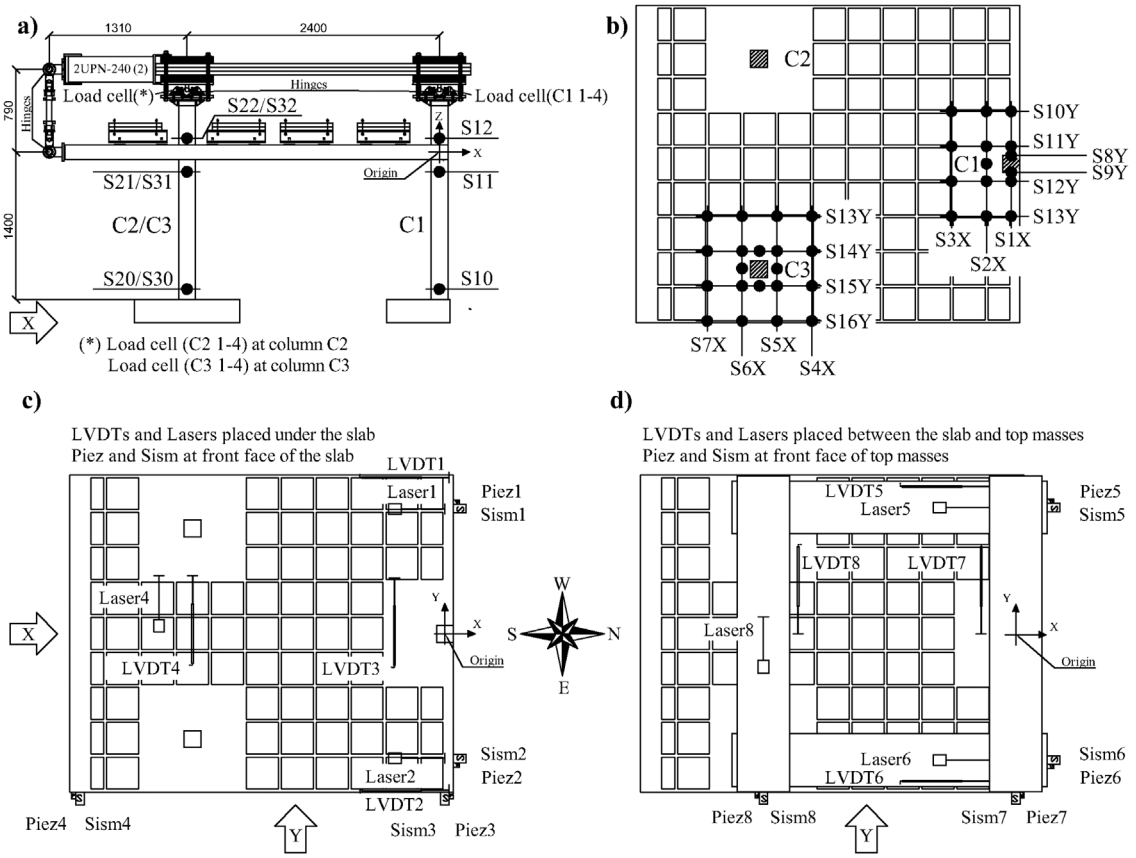

FIGURE 4 | Test setup and instrumentation: elevation (a); identification of critical regions/sections (b); and instrumentation on the RC plate (c), and on the top of the specimen (d).

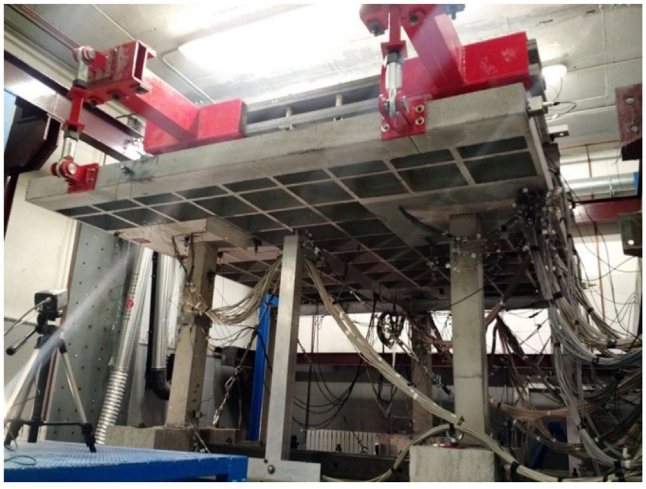

FIGURE 5 | General overview of the test specimen and setup.

TABLE 1 | Evolution of vibration periods and damping ratios.

Test	T_1 (s)	T_2 (s)	T_3 (s)	ξ (%)
Prior	0.34	0.26	0.23	2.7
B_5	0.34	0.26	0.23	2.7
B_{32}	0.34	0.26	0.23	3.2
B_{190}	0.42	0.32	0.23	3.8
B_{394}	0.46	0.35	0.27	4.6
B_{475}	0.62	0.50	0.32	5.6
B_{682}	0.75	0.52	0.36	6.5
B_{1218}	0.85	0.62	0.49	8.1

associated with a return period of 475 years. In these Figures, the dashed lines are the target spectra and the thin solid lines the actual spectra of the recorded acceleration at the base of the structure. The periods of the first, second, and third modes of vibration of the test specimen (discussed later and shown in Table 1) measured before applying the design basis earthquake are plotted in Figure 2c,d with vertical lines. It is not easy to control and accurately reproduce in experiments the high-power frequency content of near fault ground motions, especially with large payload for the hardware capabilities. This explains at least in part the differences between the target spectra and the actual ones. Nevertheless, in the range of periods of interest (between 0.27 and 0.46 s) the target and the actual spectra are reasonably close. The largest difference occurs in the very short period range (i.e., around 0.1 s). Still, these differences do not affect the response of the tested specimen because the periods that govern its response are much larger. For each test, the acceleration spectra of the motion applied at the base of the specimen in the NS and EW directions, $S_{a,NS}(T)$ and $S_{a,EW}(T)$, were computed. These pseudo accelerations were based on the recorded signals. From the $S_{a,NS}(T)$ and $S_{a,EW}(T)$ of each test, the geometric mean

10969845, 0, Downloaded from https://onlinelibrary.wiley.com/doi/10.1002/eqe.70016 by Readcube (Labtiva Inc.), Wiley Online Library on [01/07/2025]. See the Terms and Conditions (https://onlinelibrary.wiley.com/terms-and-conditions) on Wiley Online Library for rules of use; OA articles are governed by the applicable Creative Commons License

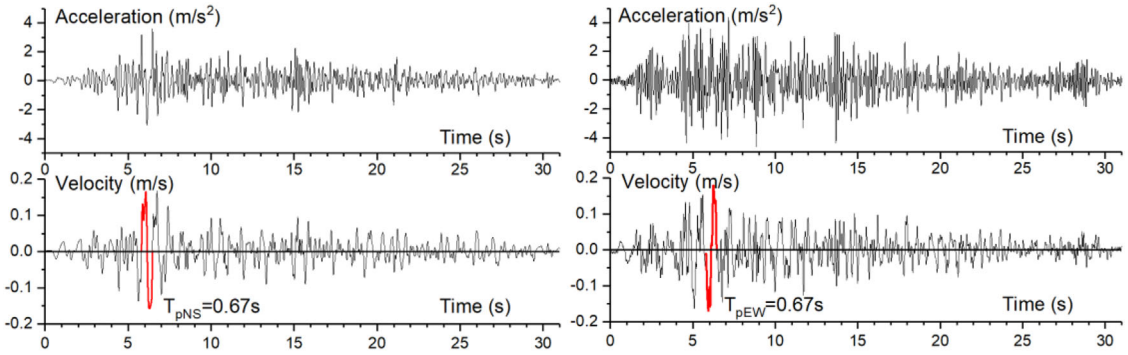

FIGURE 6 | Histories of acceleration and velocity of the NS (left) and EW (right) ground motions used in test B100.

$S_{a,GM}$ $(T) = [S_{a,NS}(T)S_{a,EW}(T)]^{0.5}$ at the fundamental period T_1 of the specimen (discussed later and shown in Table 1) was calculated giving $S_{a,GM}$ (T_1): 0.13, 0.24, 0.44, 0.56, 0.62, 0.67, 0.81 g. The response acceleration $S_{a,GM}$ (T_1) of the fifth test, i.e., 0.62 g, was very close to the response acceleration of the spectrum used in design, $S_a(T_1) = 0.60$ g. Therefore, the fifth test is taken hereafter as representing the design basis earthquake associated with a return period of 475 years and will be denoted as test B_{475}. The return period T_{RP} associated with the other tests can be estimated from the corresponding $S_{a,GM}$ (T_1) using the approximate relation $S_{a,GM}(T_1)/S_a(T_1) = (T_{RP}/475)^{(1/k)}$, where k (= 3 for moderate seismicity regions) is the slope of the seismic hazard curve for the reference response acceleration (i.e., S_a) in the logarithmic domain [2]. This gives T_{RP} = 5 years, T_{RP} = 32 years, T_{RP} = 190 years, T_{RP} = 394 years, T_{RP} = 682 years and T_{RP} = 1218 years for the tests with $S_{a,GM}$ (T_1) = 0.13, 0.24, 0.44, 0.56, 0.67, and 0.81 g, respectively, that will be referred to as tests B_5, B_{32}, B_{190}, B_{394}, B_{682}, B_{1218} hereafter. At the assumed building site, tests B_5, B_{32} represent very frequent earthquakes; B_{190} represents a frequent earthquake; test B_{394} represents an earthquake slightly below the design basis earthquake; B_{475} represents the design basis earthquake as indicated before, B_{682} represents an earthquake more severe than the design basis earthquake but below the maximum considered earthquake; B_{1218} represents a ground motion close to the maximum earthquake considered. Figure 6 depicts the histories of acceleration and velocity of the NS and EW components of the ground motions recorded on the shake table during one of the tests (B_{394}). Figure 6 indicates with a bold red line the velocity pulses whose duration was $T_{pNS} = T_{pEW} = 0.67$ s.

4 | Test Results and Interpretation

4.1 | Dynamic Characterization

Table 1 summarizes the period of the first, second, and third modes (T_1, T_2, and T_3), and the first mode damping fraction ξ. They were estimated from the transfer functions between the acceleration measured on the shake table and on the top of the specimen, during the training of the shake table with white noise (prior to testing) and at the end of each test. ξ was estimated with the half-power bandwidth method for tests B_{32} and B_{394}. In the rest of tests this method did not provide consistent results and ξ was estimated with the free-vibration decay method, using displacements measured in X and Y directions at the end of each test, when the shake table was not moving but the specimen was still vibrating. The periods T_1, T_2, and T_3 of the specimen prior to testing (i.e., 0.34, 0.26, and 0.23 s in Table 1) are close to the periods of the corresponding vibration modes in the prototype structure (0.50, 0.49, and 0.45 s) scaled by the scale factor for time 0.63, i.e., 0.32 s (= 0.50 × 0.63), 0.31 s (= 0.49 × 0.63) and 0.28 s (= 0.45 × 0.63). Based on this, it can be considered that the frequency content of the near fault excitations simulated in the shake table is close to the frequency content of the near fault excitations assumed to act on the prototype structure.

With the aid of a numerical model of the structure, it was found that the first vibration mode consisted of a translation along the Y axis combined with rotations about a vertical axis, passing through a point close to the intersection of the axis of symmetry with the line that connects columns C2 and C3. The second mode was purely translational along the X axis of symmetry. The third mode combined translations along the Y direction and rotations about a vertical axis. As seen in Table 1, T_1, T_2, T_3 did not change during tests B_5 and B_{32}, while ξ remained basically the same. This indicates that the specimen kept its initial lateral stiffness and did not experience damage under the very frequent earthquakes. After tests B_{190} and B_{394}, the fundamental period respectively increased by 24% and 36%, thus corresponding to a reduction of the lateral stiffness up to almost one half. The damping ratio also increased by 40% and 70%, respectively. This indicates that the specimen was damaged during these tests. After tests B_{475} and B_{682} the periods increased more than twofold, which means a reduction in lateral stiffness of about one-fifth, and the damping fraction increased by 40%, hence suggesting significant damage (SD). After test B_{1218} the specimen was in a very critical situation that advised discontinuing testing.

4.2 | Overall Response

The test specimen can be idealized by means of a two-mass lumped model, each with three degrees of freedom (DOF): two orthogonal translations (in X and Y directions of loading), and one rotation about a vertical axis passing through the center of mass. The DOFs 1, 2, and 3 will denote the translations along X, Y and the rotation about a vertical axis of the lower mass (i.e., the RC plate); and the DOFs 4, 5, and 6, the corresponding movements of the upper mass (i.e., the steel plates on top of

10969845, 0, Downloaded from https://onlinelibrary.wiley.com/doi/10.1002/eqe.70016 by Readcube (Labtiva Inc.), Wiley Online Library on [01/07/2025]. See the Terms and Conditions (https://onlinelibrary.wiley.com/terms-and-conditions) on Wiley Online Library for rules of use; OA articles are governed by the applicable Creative Commons License

the specimen). The lower mass (5784 kg) includes the mass of the RC elements (excepting foundations and half height of the columns of the first story) and the steel plates fixed on the plate. The upper mass (6446 kg) includes the added weight (steel plates) at the top of the specimen. The total mass of the test specimen (including the additional masses and excluding the foundation and half height of the columns of the first story) was 12,230 kg.

4.2.1 | Base Shear-Top Displacement Relationships and Capacity Curves

Using the two-mass lumped model described above, the equation of motion of the specimen is:

$$\mathbf{m}\ddot{\mathbf{u}}^{t} + \mathbf{c}\dot{\mathbf{u}} + \boldsymbol{F}_{s} = \mathbf{0} \tag{1}$$

Here, $\mathbf{m}$ is the diagonal mass matrix, $\ddot{\mathbf{u}}^{t}$ is the vector of absolute accelerations, $\mathbf{c}$ is the damping matrix, $\dot{\mathbf{u}}$ is the vector of relative velocities, and $\mathbf{F_S}$ the vector of restoring forces exerted by the structure. $\mathbf{m}$ is known and $\ddot{\mathbf{u}}^{t}$ was measured with accelerometers. The base shear force in the X and Y directions, $F_{IB,X}$ and $F_{IB,Y}$, exerted by the inertial forces $\mathbf{F_I} = \mathbf{m}\,\ddot{\mathbf{u}}^{t} = -(\mathbf{c}\,\dot{\mathbf{u}} + \boldsymbol{F}_{s})$ are given by $F_{IB,X} = \mathbf{F_I}^{\mathrm{T}}\mathbf{J}_{\mathrm{X}}$ and $F_{IB,Y} = \mathbf{F_I}^{\mathrm{T}}\mathbf{J}_{\mathrm{Y}}$, where $\mathbf{J}_{\mathrm{X}}{}^{\mathrm{T}} = [1\,0\,0\,1\,0\,0]$ and $\mathbf{J}_{\mathrm{Y}}{}^{\mathrm{T}} = [0\,1\,0\,0\,1\,0]$. Figures 7a and 8a plot $F_{IB,X}$ and $F_{IB,Y}$ against the X and Y displacement of the top of the structure, $\delta_{T,X}$ and $\delta_{T,Y}$, for all tests. At the instants when displacement is maximum, the velocity is zero and hence also the damping forces $\mathbf{c}\,\dot{\mathbf{u}}$. At these instants $F_{I,B}$ or $F_{I,B}$ are equal to the base shear force carried by the structure in the X or Y directions, Q_{BX} or Q_{BY}. For each direction X and Y, Figures 7b and 8b show with symbols the points when $\delta_{T,X}$ or $\delta_{T,Y}$ attain a maximum. In turn, the points of Figure 7b or 8b whose displacement is larger than that attained in previous cycles of displacement are connected by a bold solid line. This solid line is the "capacity curve" of the structure and it is drawn in bold red in Figures 7 and 8. The capacity curves can be further simplified with a bilinear approximation drawn with dash blue lines in Figures 7 and 8. The end points of these bilinear curves are taken as either the maximum displacements reached by the specimen during the test, or the displacement when strength drops to 80% (the smaller). The displacements corresponding to these points are understood in this study as the "ultimate displacement" capacity of the structure. The bilinear approximation is used here to define the yield base shear force Q_{BXy} and the yield top displacement δ_{TXy} in the X direction, and the counterpart values Q_{BYy} and δ_{TYy} in the Y direction. The values obtained are $Q_{BXy}{}^{+} = 45.4$ kN, $\delta_{TXy}{}^{+} = 18$ mm, $Q_{BXy}{}^{-} = 40.1$ kN, $\delta_{TXy}{}^{-} = 15.6$ mm in the X direction, and $Q_{BYy}{}^{+} = 37.2$ kN, $\delta_{TYy}{}^{+} = 13$ mm, $Q_{BYy}{}^{-} = 48.5$ kN, $\delta_{TYy}{}^{-} = 16.7$ mm in the Y direction. The corresponding base shear force coefficients in the X direction, in the positive $\alpha_{BX}{}^{+}$ and negative $\alpha_{BX}{}^{-}$ domains, are $\alpha_{BX}{}^{+} = 45.4/122.3 = 0.37$, $\alpha_{BX}{}^{-} = 40.1/122.3 = 0.33$, and in the Y direction $\alpha_{BY}{}^{+} = 37.2/122.3 = 0.30$ and $\alpha_{BY}{}^{-} = 48.5/122.3 = 0.40$. The ultimate displacements in each domain of loading are $\delta_{TXu}{}^{+} = 66.1$ mm, $\delta_{TXu}{}^{-} = 79.5$ mm in the X direction, and $\delta_{TYu}{}^{+} = 44.7$ mm, $\delta_{TYu}{}^{-} = 55.5$ mm in the Y direction. The corresponding ductility factors are $\mu_{X}{}^{+} = \delta_{TXu}{}^{+}/\delta_{TXy}{}^{+} = 66.1/18 = 3.7$, $\mu_{X}{}^{-} = \delta_{TXu}{}^{-}/\delta_{TXy}{}^{-} = 79.5/15.6 = 5.1$ in the X direction, and $\mu_{Y}{}^{+} = \delta_{TYu}{}^{+}/\delta_{TYy}{}^{+} = 44.7/13 = 3.4$, $\mu_{Y}{}^{-} = \delta_{TYu}{}^{-}/\delta_{TYy}{}^{-} = 55.5/16.7 = 3.3$ in the Y direction.

4.2.2 | Maximum Translational and Rotational Response

The maximum response of the structure expressed in terms of ID and the residual interstory drift (ID_r) have been used in the past to measure the seismic performance level (SPL) of a structure under seismic actions. SEAOC [20] proposed the following limits: ID < 0.5% and negligible ID_r for Operational (OP), 0.5 < ID ≤ 1.5% and ID_r < 0.5% for Life Safety (LS), 1.5% < ID ≤ 2.5%, and ID_r < 2.5% for Near Collapse (NC), and ID > 2.5% and ID_r > 2.5% for Collapse (C). SEAOC admitted a tolerance for these limits of ID that depends on the lateral stiffness of the structure and can be taken as ± 0.1% for WFP systems. This gives ID < 0.6% for OP, 0.6 < ID ≤ 1.6% for LS, 1.6% < ID ≤ 2.6% for NC, and ID > 2.6% for C. For each direction X and Y, Tables 2 and 3 summarize in columns 2 to 7 the values of ID and ID_r obtained from the tests, together with the absolute acceleration $\ddot{u}^{t}{}_{max}$. Columns 8 and 9 show the maximum displacement and the maximum residual displacement at the top of the specimen normalized by the total height of the specimen. Column 10 indicates the SPL according to the criterion of SEAOC. In past studies [13], the authors proposed alternative limits for these SPLs based on the results of shake table tests conducted on WFP structures subjected to far-field ground motions. These alternative limits proved to reflect better the damage observed and measured on the tested specimens, and are as follows: ID ≤ 1% for OP, 1% < ID ≤ 2.5% for LS, 2.5% < ID ≤ 4% for NC, and ID > 4% for C. The SPLs evaluated with these alternative limits are shown in column 11 of Tables 2 and 3. Table 4 displays the maximum rotational response about the center of mass. Columns 2 to 7 show the absolute angular acceleration $\ddot{u}^{t}{}_{R,max}$, the interstory rotation (IR) (relative rotation between the upper and lower level of each story), and the corresponding residual value (IR_r) at the end of the test. Columns 8 and 9 indicate the rotations at the uppermost level relative to the base.

In the 2G of Eurocode 8 [2], the seismic performance of the structure is measured by its state of damage under a given seismic action, referring to four Limit States (LS) that can be seen as the counterpart to the SPLs of SEAOC. The LS of fully Operational (OP) is defined as one in which the structure is basically undamaged, allowing for continuous operation of those systems hosted by the structure. At the LS of Damage Limitation (DL) the structure is only slightly damaged and economic to repair, with negligible permanent drifts and a limited decrease in stiffness. In turn, at the LS of SD the structure is significantly damaged; it is expected to be repairable, but in some cases may prove uneconomic to repair. At the LS of NC the structure is heavily damaged, with large permanent drifts, but retains its vertical load-bearing capacity. In case of flat slab building structures with noninteracting masonry infills, the 2G of Eurocode 8 limits the ID associated with the LS of SD to 2%, and the ID associated to the LS of DL to 1.25% if the ancillary elements attached to the structure are ductile. No quantitative limits are provided for the LS OP and for the LS of NC. The performance of the specimen under each test is discussed below in light of the above drift limits for the SPL's and the above LS definitions, together with the maximum strains measured on the longitudinal bars and the maximum chord rotations at column ends. As a result, an LS is assigned to the damage state of the specimen at the end of each test in the last column of Tables 2 and 3. Although the design of the building specimen conforms with European design codes, the

10969845, 0, Downloaded from https://onlinelibrary.wiley.com/doi/10.1002/eqe.70016 by Readcube (Labtiva Inc.), Wiley Online Library on [01/07/2025]. See the Terms and Conditions (https://onlinelibrary.wiley.com/terms-and-conditions) on Wiley Online Library for rules of use; OA articles are governed by the applicable Creative Commons License

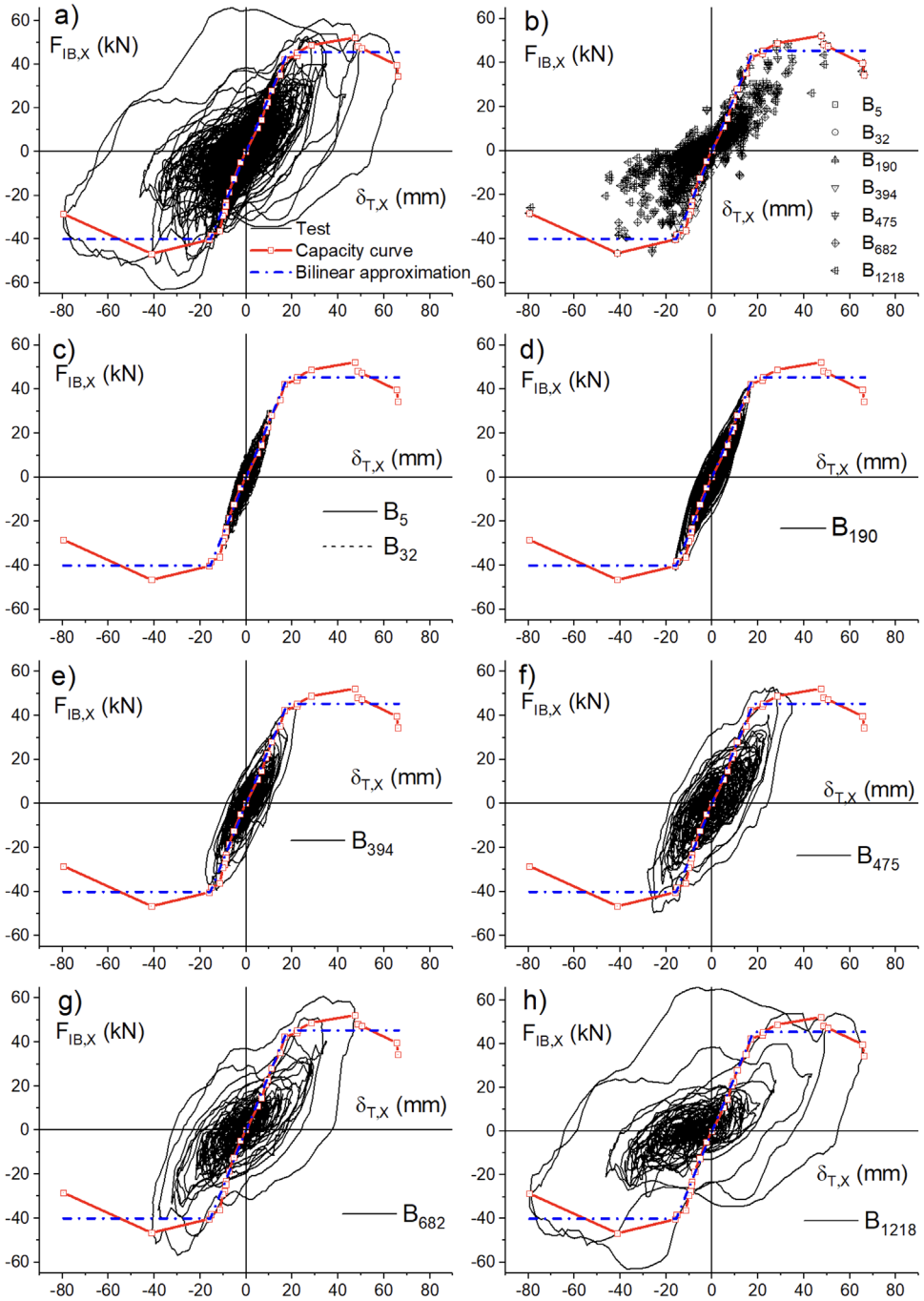

FIGURE 7 | Base shear due to inertial forces versus top displacement in direction X: (a) overall response; (b) points of zero velocity and capacity curve; (c) tests B_5, B_{32}; (d) test B_{190}; (e) B_{394}; (f) test B_{475}; (g) B_{682}; (h) test B_{1218}.

SEAOC limit states have been also considered in this study for comparison and because they use different engineering demand parameters to define quantitatively the limit states. Finally, the values of $\ddot{u}^t_{max}$ and $\ddot{u}^t_{R,max}$ in Tables 2, 3, and 4 can give an approximate idea of the floor total accelerations that can be expected in the real prototype building because the scale factor for acceleration used in the test was 1. However, this idea is only approximated since, as mentioned in Section 2.2, the tests do not reproduce the particular response that the partial structural model would experience inside the full-scale prototype buildings, that is influenced by dynamic interactions with the other parts of the structure.

4.2.3 | Response During Tests B_5 and B_{32}

Tests B_5 and B_{32} represent very frequent earthquakes. During these tests, the specimen remained elastic with maximum top displacements about one-half the yield displacement δ_{TXy}, δ_{TYy} in the X and Y directions (see Figures 7c and 8c). Hairline flexural cracks of width less than 0.1 mm were observed on the plate, at column bases, and in the transverse beams. The maximum strains ε_{max} measured on the longitudinal reinforcement at the critical sections of columns (solid circles in Figure 4a) and of the plate (solid circles in Figure 4b) remained far below the yield strain ε_y. The chord rotations at column ends were also clearly below

10969845, 0, Downloaded from https://onlinelibrary.wiley.com/doi/10.1002/eqe.70016 by Readcube (Labtiva Inc.), Wiley Online Library on [01/07/2025]. See the Terms and Conditions (https://onlinelibrary.wiley.com/terms-and-conditions) on Wiley Online Library for rules of use; OA articles are governed by the applicable Creative Commons License

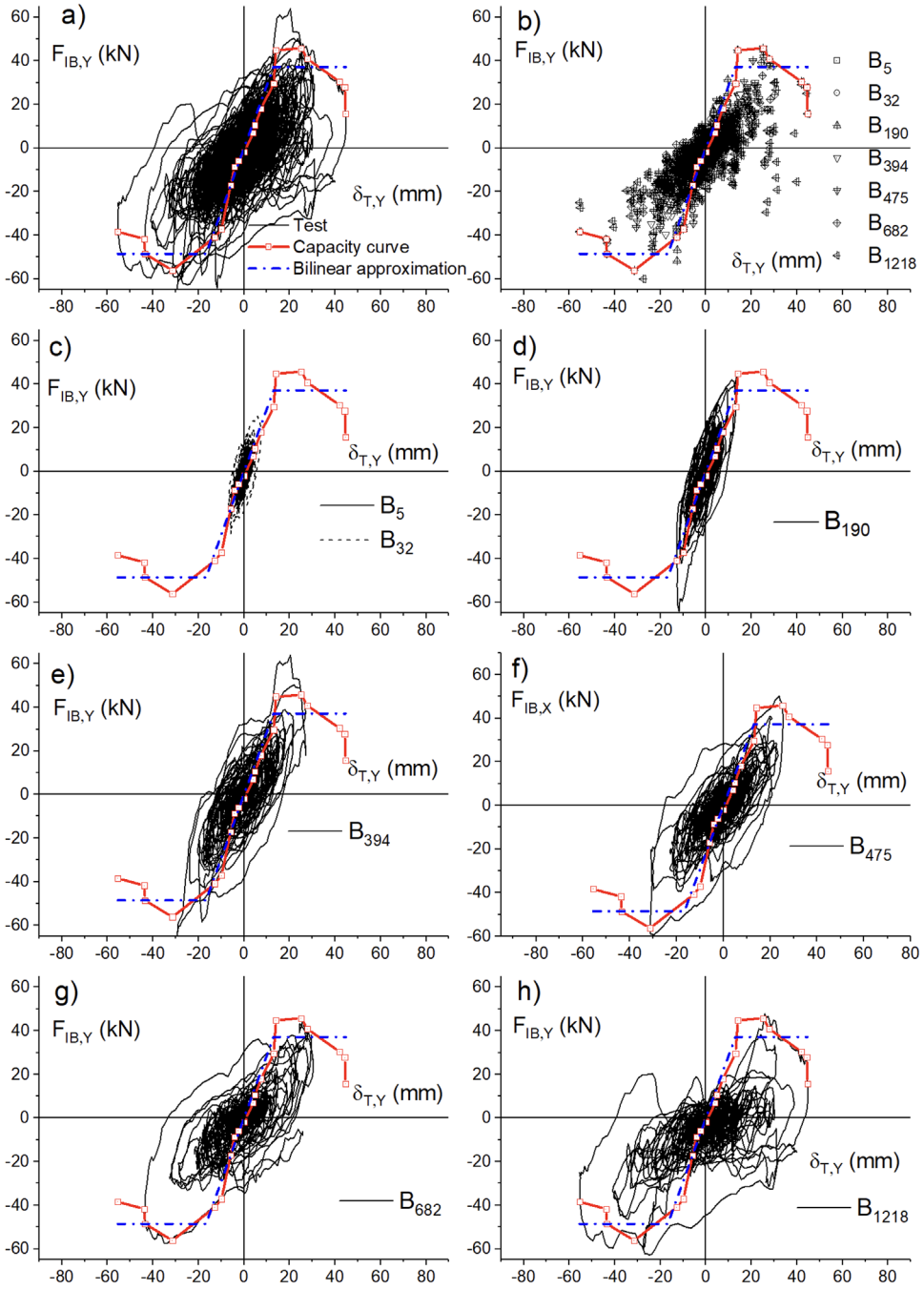

FIGURE 8 | Base shear due to inertial forces versus top displacement in direction Y: (a) overall response; (b) points of zero velocity and capacity curve; (c) tests B_5, B_{32}; (d) test B_{190}; (e) B_{394}; (f) test B_{475}; (g) B_{682}; (h) test B_{1218}.

the yield rotation θ_y, as discussed later in Section 4.5. Permanent drifts were negligible ($ID_r \leq 0.03\%$), and the maximum interstory drift was ID = 0.58%. This ID value is below the limit (0.6%) proposed by SEAOC [20] and also below the limit (1%) proposed by the authors in previous studies [13], and would correspond to SPL OP. The state of damage according to 2G of Eurocode 8 [2] can likewise be referred to LS OP.

4.2.4 | Response During Test B_{190}

Test B_{190} represents an earthquake close (yet slightly more intense) to the frequent earthquake that 2G of Eurocode 8 [2] characterizes with a return period $T_{RP} = 115$ years for a building of consequence class CC2, associated with the LS of DL. During this test, the structure was slightly damaged. The top displacements of the structure did not exceed the yield displacements δ_{TXy}, δ_{TYy} in the X and Y directions, as shown in Figures 7d and 8d. Minor concrete cracks of width less than 0.1 mm were observed at column bases. At the base of column C1 (section S10 in Figure 4a), $\varepsilon_{max} < 0.6\varepsilon_y$ in most rebars and very few of them approached ε_y. At the base of columns C2 and C3 (sections S20 and S30 in Figure 4a), ε_{max} exceeded ε_y but kept below $2\varepsilon_y$. At the top end of column C1 in the first story (section S11 in Figure 4a), ε_{max} remained below ε_y, while at the sections located at the same level in columns C2 and C3 (sections S21 and S31 in Figure 4a) it reached $\varepsilon_{max} = 1.9\varepsilon_y$. At the

10969845, 0, Downloaded from https://onlinelibrary.wiley.com/doi/10.1002/eqe.70016 by Readcube (Labtiva Inc.), Wiley Online Library on [01/07/2025]. See the Terms and Conditions (https://onlinelibrary.wiley.com/terms-and-conditions) on Wiley Online Library for rules of use; OA articles are governed by the applicable Creative Commons License

TABLE 2 | Maximum translational response in X direction.

	Story 1			Story 2			Top		Seismic performance		
Test	$\ddot{u}^t_{max}$ (g)	ID (%)	ID_r (%)	$\ddot{u}^t_{max}$ (g)	ID (%)	ID_r (%)	ID (%)	ID_r (%)	SPL SEAOC	SPL Ref. [21]	LS EN1998
B_5	0.23	0.48	0.00	0.25	0.43	0.00	0.46	0.00	OP	OP	OP
B_{32}	0.30	0.57	0.00	0.30	0.58	0.03	0.55	0.01	OP	OP	OP
B_{190}	0.31	0.85	0.02	0.40	0.84	0.05	0.83	0.00	LS	OP	DL
B_{394}	0.42	1.17	0.05	0.46	0.99	0.16	1.11	0.02	LS	LS	SD
B_{475}	0.47	1.87	0.07	0.55	1.42	0.03	1.72	0.04	NC	LS	SD
B_{682}	0.55	2.55	0.11	0.59	1.91	0.21	2.35	0.14	NC	NC	NC
B_{1218}	0.56	4.01	0.42	0.60	3.88	0.98	3.94	0.59	C	C	C

SPL, seismic performance level; O, Operational; LS, life safety; NC, near collapse; C, collapse.

TABLE 3 | Maximum translational response in Y direction.

	Story 1			Story 2			Top		Seismic performance		
Test	$\ddot{u}^t_{max}$ (g)	ID (%)	ID_r (%)	$\ddot{u}^t_{max}$ (g)	ID (%)	ID_r (%)	ID (%)	ID_r (%)	SPL SEAOC	SPL Ref. [21]	LS EN1998
B_5	0.15	0.30	0.00	0.17	0.23	0.01	0.29	0.00	OP	OP	OP
B_{32}	0.27	0.43	0.00	0.21	0.31	0.03	0.37	0.01	OP	OP	OP
B_{190}	0.69	0.94	0.00	0.42	0.55	0.03	0.69	0.01	LS	OP	DL
B_{394}	0.41	1.48	0.01	0.56	1.23	0.11	1.46	0.04	LS	LS	SD
B_{475}	0.47	1.69	0.04	0.58	1.24	0.09	1.56	0.06	NC	LS	SD
B_{682}	0.44	2.43	0.06	0.83	1.56	0.00	2.17	0.04	NC	LS	NC
B_{1218}	0.87	3.13	0.04	0.90	1.72	0.23	2.75	0.12	C	NC	C

TABLE 4 | Maximum rotational response around the center of mass.

	Story 1			Story 2			Top	
Test	$\ddot{u}^t_{R,max}$ (rad/s^2)	IR (rad) 10^{-3}	IR_r(rad) 10^{-3}	$\ddot{u}^t_{R,max}$ (rad/s^2)	IR (rad) 10^{-3}	IR_r (rad) 10^{-3}	IR (rad) 10^{-3}	IR_r (rad) 10^{-3}
B_5	0.71	2.37	0.03	0.91	0.93	0.01	3.25	0.02
B_{32}	1.65	4.72	0.04	2.03	1.71	0.11	6.33	0.06
B_{190}	2.09	7.05	0.05	3.04	3.18	0.28	9.99	0.23
B_{394}	2.55	7.27	0.05	2.17	4.00	0.97	10.64	0.92
B_{475}	1.82	9.92	0.38	2.66	4.91	0.97	14.73	1.35
B_{682}	1.82	9.27	0.18	1.73	4.81	0.55	13.46	0.37
B_{1218}	1.70	15.16	1.11	2.50	6.06	0.16	20.53	1.27

bottom end of the columns of the second story (sections S12, S22, and S32 in Figure 4a), ε_{max} remained below ε_y, being about two times larger in columns C2 and C3 ($\varepsilon_{max} \leq 0.7\varepsilon_y$) than in column C1 ($\varepsilon_{max} \leq 0.35\varepsilon_y$). The larger plastic deformation demands in columns C2 and C3 in comparison with C1 is most probably due to the rotational movement of the specimen about a vertical axis close to column C1. The longitudinal reinforcement of (i) the transverse beams at the critical sections S8Y and S9Y in Figure 4b, (ii) of the plate around column C1 at sections S1X to S3X and S10Y to S13Y in Figure 4b, and (iii) of the plate around column C3 at sections S4X to S7X and S13Y to S16Y in Figure 4b did not yield, reaching $\varepsilon_{max} \leq 0.6\varepsilon_y$, $\varepsilon_{max} \leq 0.4\varepsilon_y$ and $\varepsilon_{max} \leq 0.7\varepsilon_y$, respectively. During test B_{190} the maximum IDs varied in the range $0.83\% \leq ID \leq 0.94\%$, and the permanent drifts were small ($ID_r \leq 0.05\%$). Applying SEAOC [20] criteria these ID's correspond to an SPL of LS, but applying the criteria proposed by the authors in previous studies [13] the SPL is OP. The second criterion is judged more appropriate in view of (i) the slight damage observed, (ii) the small

10969845, 0, Downloaded from https://onlinelibrary.wiley.com/doi/10.1002/eqe.70016 by Readcube (Labtiva Inc.), Wiley Online Library on [01/07/2025]. See the Terms and Conditions (https://onlinelibrary.wiley.com/terms-and-conditions) on Wiley Online Library for rules of use; OA articles are governed by the applicable Creative Commons License

strains measured in the gauges, and (iii) the fact that the chord rotations at column ends remained below the yield rotation θ_y, yet close to it, as discussed later in Section 4.5. The state of damage according to 2G of Eurocode 8 [2] should be referred to the LS of DL since the specimen was only slightly damaged, ε_y and θ_y were not exceeded and the ID limit of 1.25% was not exceeded.

4.2.5 | Response During Test B_{394}

Test B_{394} represents an earthquake notably more severe than the frequent earthquake (T_{RP} = 115 years) and near (yet below) the design earthquake that 2G of Eurocode 8 [2] characterizes with a return period of 475 years for a building of consequence class CC2, and associates with the LS of SD. In this test the specimen endured SD. Flexural cracks were observed at column ends. Torsional cracks and concrete spalling were also noticeable in the transverse beams. The top displacement of the structure in the Y direction exceeded the yield displacements δ_{TYy} by about 80%, as shown in Figure 8e, while in the X direction it remained very close to the yield displacement δ_{TXy}. The longitudinal reinforcement of the three columns yielded at the base (sections S10, S20, S30 in Figure 4a). In column C1 ε_{max} reached $2\varepsilon_y$ in most rebars, while in columns C2 and C3 ε_{max} attained $3\varepsilon_y$. At the top end of column C1 in the first (ground) story (section S11 in Figure 4a), ε_{max} remained below ε_y ($\varepsilon_{max}<0.7\varepsilon_y$), whereas at the sections located at the same level in columns C2 and C3 (sections S21 and S31 in Figure 4a) ε_{max} reached $\varepsilon_{max} = 3.6\varepsilon_y$. In the second story, the longitudinal reinforcement of the bottom end of column C1 (section S12 in Figure 4a) remained elastic ($\varepsilon_{max}\leq 0.3\varepsilon_y$), yet in the other columns (sections S22 and S32 in Figure 4a) ε_{max} reached ε_y. Again, these differences of ε_{max} among column C1 and columns C2-C3 can be attributed to torsional effects. The longitudinal reinforcement of the transverse beams at the critical sections S8Y and S9Y (Figure 4b) in the vicinity of column C1 exceeded ε_y. In contrast, the longitudinal rebars of the plate around columns C2 and C3 remained elastic ($\varepsilon_{max} \leq 0.6\varepsilon_y$). This means that during tests B_{394}, the exterior plate–column connection developed a strong column-weak plate mechanism, while the interior plate–column connection exhibited a weak column-strong plate mechanism. During test B_{394}, the ID was in the range $0.99 \leq ID \leq 1.48$ and the residual drift reached ID_r = 0.16%. Applying SEAOC [20] criteria or the criterion proposed by the authors in previous studies [13], this response corresponds to an SPL of LS. In all columns the chord rotations exceed the yield rotation θ_y by up to 60%, remaining below, yet close to, the limit $\theta_{SD} = [\theta_y + 0.5(\theta_u - \theta_y)] / \gamma_{Rd,SD}$ that 2G of Eurocode 8 [2] associates with the attainment of the LS of SD, as discussed later in Section 4.5. Here, $\gamma_{Rd,SD}$ is a partial factor that 2G of Eurocode 8 recommends taking as $\gamma_{Rd,SD}$ = 1.35. The state of damage according to 2G of Eurocode 8 should be referred to the LS of SD since the specimen was significantly damaged, the chord rotations were between θ_y and θ_{SD}, and the maximum ID (1.48%) was between 1.25% and 2%.

4.2.6 | Response Under Test B_{475}

Test B_{495} represents the design basis earthquake that 2G of Eurocode 8 [2] characterizes with a return period T_{RP} = 475 for buildings of consequence class CC2, and associates with the LS of SD as indicated above. The damage at the end of the tests was significant, involving an increased width of previous cracks and the appearance of new ones, together with concrete spalling at column ends and at transverse beams. The top displacement of the structure in both X and Y directions clearly exceeded the yield displacements δ_{TXy} and δ_{TYy}. While in the Y direction the maximum top displacements were very similar to those of previous test B_{394}, in the X direction the increase was significant, reaching up to $1.9\delta_{TXy}$. At the base of the three columns, ε_{max} exceeded ε_y in all rebars and reached $7\varepsilon_y$ in some of them. At the top end of all columns of the first (ground) story (section S11, S21, S31 in Figure 4a), ε_{max} exceeded ε_y —being $\varepsilon_{max}<1.1\varepsilon_y$ in columns C1 and C2 and reaching $\varepsilon_{max} = 6\varepsilon_y$ in column C3. At the bottom end of the columns of the second story (sections S12, S22, and S32 in Figure 4a), ε_{max} remained below ε_y ($\varepsilon_{max}\leq 0.5\varepsilon_y$) in column C1, and slightly exceeded ε_y ($\varepsilon_{max}\leq 1.1\varepsilon_y$) in columns C2 and C3. The longitudinal reinforcement of the transverse beams at the critical sections S8Y and S9Y (Figure 4b) yielded, reaching large plastic deformations up to $\varepsilon_{max} = 10\varepsilon_y$. The longitudinal rebars of the plate around columns C1 and C3 approached ε_y and few bars yielded ($\varepsilon_{max}\leq 3\varepsilon_y$). The maximum chord rotations in all column ends exceeded the yield rotation θ_y and were very close to θ_{SD}, as discussed later in Section 4.5. In one plastic excursions the maximum rotation exceeded θ_{SD}, but not by more than 15% and always below the rotation $\theta_{NC}=\theta_u / \gamma_{Rd,NC}$ that 2G of Eurocode 8 [2] associates with the attainment of the LS NC, as discussed later in Section 4.5. Here, $\gamma_{Rd,NC}$ is a partial factor that 2G of Eurocode 8 [2] recommends taking as $\gamma_{Rd,NC}$ = 1.60. The maximum IDs were in the range $1.24\% \leq ID \leq 1.87\%$ and the permanent drifts were $ID_r \leq 0.09$. Applying SEAOC criteria [20], the SPL is NC. According to the criteria proposed by the authors in previous studies [13], the SPL is LS. The latter appraisal seems more appropriate since (i) the capacity curves in the X and Y directions (Figures 7f and 8f) do not show any drop in lateral strength, and (ii) the maximum chord rotations in most column ends remained below θ_{SD}. For the same reasons and because the maximum ID (1.87%) was between 1.25% and 2%, the state of damage according to 2G of Eurocode 8 [2] should be referred to the LS of SD.

4.2.7 | Response Under Test B_{682}

Test B_{682} is a seismic action more severe than the design basis earthquake associated with T_{RP} = 475 years, but below the maximum considered earthquake that 2G of Eurocode 8 characterizes with a return period of 1600 years for buildings of consequence class CC2 and associates with the LS of NC. After tests B_{682} the specimen was heavily damaged. Concrete spalling continued at the base of the three columns. The torsional cracks extended, and concrete spalling continued also in the transverse beams of the exterior connection as shown in Figure 9a. The base shear-top displacement curve in the X direction (Figure 7e) shows a drop of lateral strength on the capacity curve, yet it is moderate, that is, less than the 20% normally associated with the attainment of the ultimate state of the structure. ε_{max} exceeded ε_y at the ends of all columns of both stories. All the longitudinal reinforcement of the transverse beams at the critical sections S8Y and S9Y (Figure 4b) yielded, reaching plastic deformations up to $\varepsilon_{max} = 12\varepsilon_y$. Several longitudinal rebars of the plate around columns C1 and C3

10969845, 0, Downloaded from https://onlinelibrary.wiley.com/doi/10.1002/eqe.70016 by Readcube (Labtiva Inc.), Wiley Online Library on [01/07/2025]. See the Terms and Conditions (https://onlinelibrary.wiley.com/terms-and-conditions) on Wiley Online Library for rules of use; OA articles are governed by the applicable Creative Commons License

FIGURE 9 | Exterior plate–column connection at the end of test: (a) B_{682}; (b) B_{1218}.

yielded and some reached plastic deformations up to $\varepsilon_{max} \leq 4.5\varepsilon_y$. The maximum IDs reached 2.55%, and the permanent drifts almost 0.21%. As for the maximum chord rotations at column ends, θ_{SD} was exceeded in several cycles by up to 47%; in two plastic excursions it slightly exceeded θ_{NC}, as discussed later in Section 4.5. Applying SEAOC criteria [20] or the criteria proposed by the authors in previous studies [13], the SPL is NC. The state of damage according to 2G of Eurocode 8 should also be referred to the LS of NC, since the specimen was heavily damaged the chord rotations at column ends were between θ_{SD} and θ_{NC} and the maximum ID (2.55%) exceeded the limit of 2%. The state of damage cannot be considered as LS of C because the drop of lateral strength was less than 20% and the chord rotations at column remained below θ_{NC}.

4.2.8 | Response Under Test B_{1218}

Test B_{1218} is a seismic action close to the maximum considered earthquake that 2G of Eurocode 8 characterizes with a return period of 1600 years for buildings of consequence class CC2 and associates with the LS of NC. After this test the specimen was in a very critical state. Damage was particularly heavy in the exterior connection as shown in Figure 9b, where the plate was hanging from the column with the shear forces transferred basically by the dowel action of the longitudinal reinforcement crossing the plate-column interface. In all the column the chord rotations exceeded θ_{NC} by up to 58% and came very close to θ_u. The base shear-top displacement relationships (Figures 7h and 8h) show a severe drop in lateral strength on the capacity curves, of about 35% in the X direction and 70% in the Y direction. The maximum IDs exceeded 4% and the permanent drifts approached 1%. According to SEAOC criteria [20] or the criteria proposed by the authors in previous studies [13], the SPL is C. According to 2G of Eurocode 8 the LS of SD was clearly exceed since the maximum ID was larger than 2%.

4.3 | Energy Dissipation at Global Level

Equation (2) shows the energy balance of the structure subjected to the NS and EW components of the ground motion. E_I is, by definition, the relative energy input by the earthquake; W_ξ is the energy dissipated by the inherent damping mechanism; W_p is the hysteretic (plastic strain) energy; W_{es} is the elastic strain energy; and W_k is the kinetic energy. The elastic vibrational energy W_e is by definition W_e (= W_{es} + W_k).

$$E_I = W_\xi + W_p + W_{es} + W_k \tag{2}$$

E_I and W_k can be easily calculated at each instant t by Equations (3) and (4), since the mass matrix $\mathbf{m}$ is known, and the relative displacements $\mathbf{u}$ and the absolute accelerations $\ddot{u}_{gX}$, $\ddot{u}_{gY}$ were measured during the tests. E_I is the sum of the energy input in the X, E_{IX}, and Y, E_{IY} directions.

$$E_I = E_{IX} + E_{IY} = \int_0^t \left\{\dot{\mathbf{u}}^{\mathrm{T}}\mathbf{m}\mathbf{J}_X\ddot{u}_{gX}\right\} dt + \int_0^t \left\{\dot{\mathbf{u}}^{\mathrm{T}}\mathbf{m}\mathbf{J}_Y\ddot{u}_{gY}\right\} dt \tag{3}$$

$$W_k = \frac{1}{2}\sum_{i=1}^{6} m_i\dot{u}_i^2 \tag{4}$$

In Equation (4), m_i designates the diagonal components of $\mathbf{m}$ and $\dot{u}_i$ —the derivate with respect to time of the components of $\mathbf{u}$. Once E_I and W_k are calculated, $W_\xi + W_p + W_{es}$ (= $E_I - W_k$) can be readily obtained from Equation (2). Figure 10a shows with thin lines a zoom of a typical history of ($W_\xi + W_p + W_{es}$). The recoverable elastic strain energy W_{es} causes oscillations on the curve that can be removed by taking the minimum envelope of the history of $W_\xi + W_p + W_{es}$, and the resulting curve (bold line in Figure 10a) is the history of the total absorbed energy ($W_\xi + W_p$). By proceeding in this way, the history of ($W_\xi + W_p$) accumulated during all tests was obtained. The difference between the thin line and the bold line in Figure 10a is the elastic strain energy of W_{es} that was also calculated and added to W_k to obtain the total elastic vibrational energy W_e (= W_{es} + W_k). The history of ($W_\xi + W_p$) is drawn in Figure 10b together with E_I, E_{IX}, and E_{IY}. It can be seen that E_I and ($W_\xi + W_p$) are almost coincident, because the elastic vibrational energy W_e (= $W_{es} + W_k$) becomes negligible in comparison with E_I when the structure starts to dissipate energy through plastic deformations. The vertical axis indicates the total input energy accumulated up to the end of each test, along with the increment of total input energy from one test to the next. Figure 10b also shows that the total energy input in the Y direction was about 20% larger than in the X direction.

The total absorbed energy (W_p + W_ξ) includes the energy dissipated by inherent viscous damping, W_ξ. When the structure undergoes large plastic deformations it is not possible to determine W_ξ with accuracy, because it is hard to distinguish it from the energy loss due to the plastic deformations of members. An attempt was nonetheless made to obtain a rough estimation of W_ξ using the two-mass lumped model explained in Section 4.2, as follows. The inherent viscous damping was represented by a damping matrix $\mathbf{c}$ proportional to the mass matrix $\mathbf{m}$, i.e, $\mathbf{c} = a_o\mathbf{m}$, and the parameter a_o was determined so that the damping ratio for the fundamental mode of frequency ω_1 (= $2\pi/T_1$ = 18.5 rad/s) equals the initial damping ratio ξ (= 2.7%) given in Table 1, that

10969845, 0, Downloaded from https://onlinelibrary.wiley.com/doi/10.1002/eqe.70016 by Readcube (Labtiva Inc.), Wiley Online Library on [01/07/2025]. See the Terms and Conditions (https://onlinelibrary.wiley.com/terms-and-conditions) on Wiley Online Library for rules of use; OA articles are governed by the applicable Creative Commons License

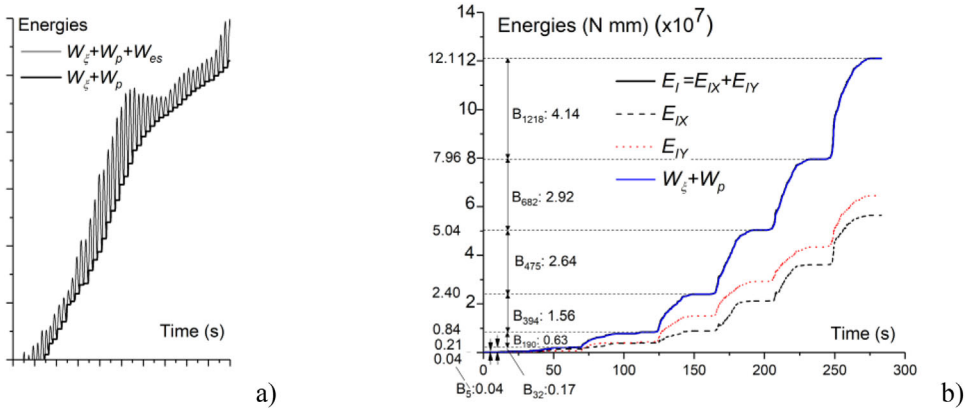

FIGURE 10 | Histories of accumulated input energy in X and Y directions (a) and typical history of $W_\xi + W_p + W_{es}$ (b).

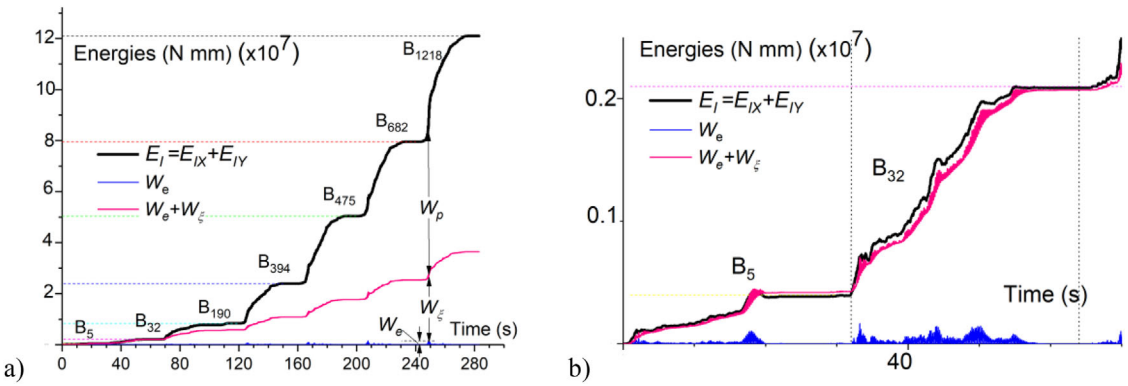

FIGURE 11 | Distribution of the total input energy E_I among W_ξ, W_p, and W_e for all tests (a), and for tests B_5, B_{32} (b).

is, $a_o = 2\xi\omega_1$. The components $\dot{u}_i$ of the relative velocity vector $\dot{\mathbf{u}}$ were obtained by deriving the histories of displacement provided by the instrumentation. Noting that $\mathbf{m}$ is a diagonal matrix whose terms are named m_i, the energy dissipated by inherent damping up to a given instant t is simply:

$$W_\xi = \int_0^t \dot{\mathbf{u}}^T \mathbf{c}\dot{\mathbf{u}}\mathrm{d}t = 2\xi_1\omega_1 \sum_{i=1}^{6} \int_0^t m_i \dot{u}_i^2 dt \tag{5}$$

The history of W_ξ estimated in this way —accumulated throughout the successive tests and summed up to elastic vibrational energy W_e— is shown in Figure 11a. As already pointed out, W_e is negligible in comparison to the rest of the energies. The difference between E_I and $(W_\xi + W_e)$ is the energy dissipated through plastic deformations by the structure W_p $(= E_I - W_\xi - W_e)$. Further, $E_D = W_p + W_e$ is what Housner [22] called the "energy that contributes to damage." Figure 11b depicts a zoom of Figure 11, focused on tests B_5 and B_{32}, for which the specimen remained elastic. For these tests the curves E_I and $(W_\xi + W_e)$ are basically coincident, thus indicating that the approach applied to estimate W_ξ gives consistent results. Table 5 summarizes the evolution of E_I and E_D, likewise expressed in terms of equivalent velocities defined by $V_E = \sqrt{2E_I/M}$ and $V_D = \sqrt{2E_D/M}$. In Table 5, ΔE_I, ΔE_D denote the increments of energy of each test, and E_I, E_D, V_E, V_D the accumulated values from the beginning of the tests. It is worth noting that the total (accumulated) energy input by the two components of the near-fault ground motion to the structure when it collapsed, expressed in terms of equivalent velocity (4.44 m/s in Table 5), is close to the value obtained in previous studies [13] on a similar specimen tested with a shake table under two components of a far-field ground motion (3.82 m/s), and also close to the value obtained in previous studies [12] on a similar specimen tested under one single component of a far-field earthquake (3.95 m/s). This would suggest that the ultimate energy dissipation capacity of the structure is basically independent of the type of ground motion (near-fault or far-field), and independent of whether one or two components of the ground are applied.

Several relevant features can be derived from Figure 11 and Table 5. First, the portion of the total input energy E_I dissipated by inherent damping, W_ξ, decreases significantly as the structure undergoes larger plastic deformation (see column 8 of Table 5). This feature was already noted in past studies [21]. At the end of the last test, W_ξ represents only 30% E_I; the rest of the energy (basically W_p) was invested in damaging the structure. Second, the formula proposed by Akiyama [21] to predict the ratio $V_D/V_E(= [1/(1 + 3\xi + 1.2\sqrt{\xi})])$ in structures subjected to large plastic deformations demands, specialized for $\xi = 0.027$, gives $V_D/V_E = 0.78$. This value is close to the results obtained in tests B_{475} to B_{1218}, in which the specimen largely entered the nonlinear range. Past studies [21] showed that given an earthquake, the energy input per unit mass depends almost exclusively on the structure's fundamental period, and it is roughly independent of the viscous damping ratio, the postyield hardening ratio, the

10969845, 0, Downloaded from https://onlinelibrary.wiley.com/doi/10.1002/eqe.70016 by Readcube (Labtiva Inc.), Wiley Online Library on [01/07/2025]. See the Terms and Conditions (https://onlinelibrary.wiley.com/terms-and-conditions) on Wiley Online Library for rules of use; OA articles are governed by the applicable Creative Commons License

TABLE 5 | Evolution of energies.

Test	E_I [kNm]	V_E [cm/s]	E_D [kNm]	V_D [cm/s]	ΔE_I [kNm]	ΔE_D [kNm]	$\frac{W_\xi}{E_I}$	$\frac{E_D}{E_I}$	$\frac{V_D}{V_E}$
B_5	0.38	25.08	0.00	0.00	0.38	0.00	1.00	0.00	0.00
B_{32}	2.09	58.47	0.02	5.73	1.71	0.02	0.99	0.01	0.10
B_{190}	7.76	112.66	2.17	59.57	5.67	2.15	0.72	0.28	0.53
B_{394}	23.98	198.03	13.11	146.41	16.22	10.94	0.45	0.55	0.74
B_{475}	50.44	287.22	32.69	231.21	26.46	19.58	0.35	0.65	0.80
B_{682}	79.57	360.74	54.23	297.79	29.13	21.54	0.32	0.68	0.83
B_{1218}	121.03	444.88	84.62	372.00	41.46	30.39	0.30	0.70	0.84

degree of inelastic action, the number of degrees of freedom, the structural type, or other characteristics of the structure. The fundamental period of the test specimen, 0.34 s, was very close to the fundamental period of the prototype building scaled by the scale factor for time 0.32 s (= 0.5 × 0.63). This ensures that the energy input from the recorded ground motion acting on the tested structure correctly reflects the energy input of the near fault ground motion acting on the full-scale building system. The energy input E_I associated with the recorded base acceleration expressed in terms of V_E can be related with the input energy of the real prototype building $E_{I,prototype}$, expressed in terms of equivalent velocity $V_{E,prototype}(=\sqrt{2E_{I,prototype}/M_{prototype}})$, by $V_E = V_{E,prototype}\sqrt{\lambda_L\lambda_a}$, where $M_{prototype}$ is the total mass of the prototype building, and the scale factors for length and for acceleration in this study are $\lambda_L = 2/5$ and $\lambda_a = 1$.

4.4 | Energy Dissipation at Local Level

4.4.1 | Energy Stored/Dissipated by Columns

The elastic strain energy, $W_{es,k}$, and the plastic strain energy, $W_{p,k}$, stored and dissipated, respectively, in a plastic hinge k of a column, from instant $t = 0$ to $t = t_t$, can be obtained by summing up the energy stored/dissipated by concrete, $W_{C,k}$, and by steel rebars, $W_{S,k}$ [23]. It is considered here that the plastic hinge is delimited by two parallel planes perpendicular to the longitudinal reinforcement and spaced a distance l_p (= h in this study). $W_{C,k}$ and $W_{S,}$ are estimated neglecting the shear deformations, as follows. The cross-section of the plastic hinge, of depth h and width b, is divided in N×N fibers of depth h/N and width b/N. A different material (steel or concrete) is assigned to each fiber. The strain at any instant t, $\varepsilon_{Sr}(t)$, of any other rebar r of the cross-section of the plastic hinge is calculated from the strains measured by the gauges adhered to the longitudinal reinforcement. The stress $\sigma_{Sr}(t)$ associated with $\varepsilon_{Sr}(t)$ is estimated using an energy conservative steel constitutive model that incorporates strain-hardening and Bauschinger effects. Calling A_{Sr} the area of a rebar r and assuming that plastic deformation develops uniformly in the length l_p, $W_{S,k}$ at a given instant t is obtained as follows:

$$W_{S,k} = \sum_{r=1}^{R} \int_{\varepsilon_{sr}(0)}^{\varepsilon_{sr}(t_t)} l_p A_{sr} \sigma_{sr} d\varepsilon_{sr} \tag{6}$$

where R is the number of longitudinal rebars of length l_p. On the other hand, assuming that there is no slippage between longitudinal rebars and the surrounding concrete, and assuming the plane sections remain plane after bending, it is possible to calculate the strain $\varepsilon_{Cj}(t)$ at a given concrete fiber j of the cross-section from the strains $\varepsilon_{Sr}(t)$ provided by the longitudinal rebars. The corresponding stress, $\sigma_{Cj}(t)$, is estimated from $\varepsilon_{Cj}(t)$ using a Maekawa material model [24] for concrete. In this model, the tensile strength of the concrete is neglected for the sake of simplicity. Finally, assuming that plastic deformation develops uniformly in the length l_p, $W_{C,k}$ at a given instant, t is obtained as follows:

$$W_{C,k} = \sum_{concrete\ fibers} \int_{\varepsilon_{sr}(0)}^{\varepsilon_{sr}(t_t)} l_p \frac{b}{N} \frac{h}{N} \sigma_{Cj} d\varepsilon_{Cj} \tag{8}$$

where the summation extends to all concrete fibers of the cross-section. The elastic and plastic strain energy stored/dissipated by a given plastic hinge k is thus:

$$W_{es,k} + W_{p,k} = W_{S,k} + W_{C,k} \tag{9}$$

Figure 12 shows the energy stored/dissipated by the plastic hinges at column ends obtained by applying the above procedure, up to the end of test B_{682}. It was not possible to obtain the energies for test B_{1218} because many of the strain gauges failed during this test. Several features deserve attention. First, the amount of energy stored/dissipated at the bottom and top ends of the columns of the first story (Figure 12a,b) is similar, and much larger (about 10 times) than the energy stored/dissipated at the bottom end of the columns of the second story (Figure 12c). Since the oscillating part of the curves is due to the recoverable elastic strain energy, the fact that the curves in Figure 12a,b increase almost monotonically means that at the bottom and top ends of the columns of the first story most of the energy is dissipated through plastic deformations, which involves damage. In contrast, the curves of Figure 12c are highly oscillating, this meaning that at the bottom end of the columns of the second story most of the energy is stored in the form of elastic deformations and the damage is low. Second, at the end of test B_{682}, the energy absorbed/dissipated by the columns represents about 5% of the total input energy E_I, and 7.4% of the energy that contributes to damage E_D. Third, focusing on the first story (Figures 12a,b), it can be seen that the amount of energy dissipated by each column is in general different due to torsion effects and the

10969845, 0, Downloaded from https://onlinelibrary.wiley.com/doi/10.1002/eqe.70016 by Readcube (Labtiva Inc.), Wiley Online Library on [01/07/2025]. See the Terms and Conditions (https://onlinelibrary.wiley.com/terms-and-conditions) on Wiley Online Library for rules of use; OA articles are governed by the applicable Creative Commons License

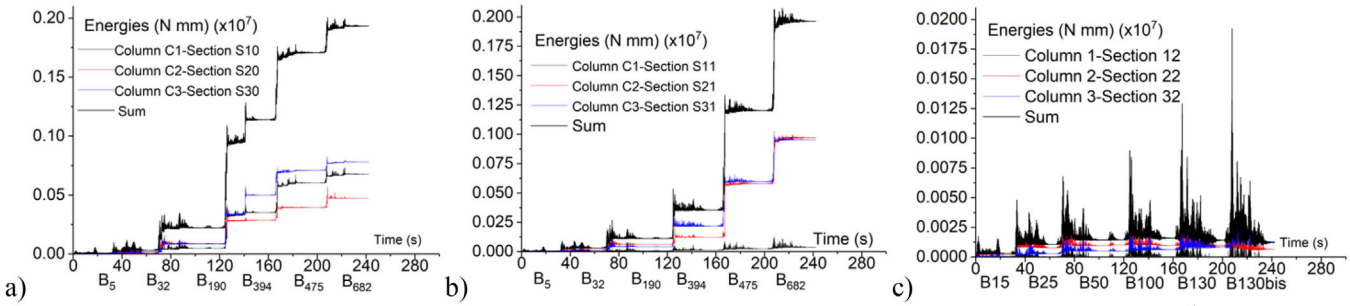

FIGURE 12 | Energy stored/dissipated by columns at the base (a), at top 1st story (b), and at bottom 2nd story (c).

bidirectional seismic action. Nonetheless, a common pattern for the distribution of energies among the columns is observed along the tests. Focusing on the hinges located at the bottom end of the columns of the first story (Figure 12a), the interior column C3 is the one that dissipates more energy and the interior column C2 the least; as the severity of the seismic action increases, the amount of energy dissipated by the three columns tend to coincide. Focusing on the hinges located at the top end of the columns of the first story (Figure 12b), the interior columns (C2 and C3) dissipate much more energy than the exterior one (C1) in all tests.

4.4.2 | Energy Dissipated by the Waffle-Flat Plate

The energy stored and dissipated by the plastic hinges located at column ends can be directly calculated from the strains measured by the gauges because the ends of the columns are fully instrumented with strain gauges, the plastic hinge region is well defined, and most energy is dissipated by bending. On the contrary, the energy stored and dissipated by the waffle-flat plate cannot be evaluated directly with the data provided by the instrumentation for several reasons. One is that the geometry of the regions of potential plastic deformations cannot be clearly defined, that is, the concept of "plastic hinge" of length l_p developed for linear —frame— members is not directly applicable to bidimensional plate elements. Another reason is that the plate dissipated most of the energy in the transverse beams of the exterior connection under torsional deformations, as shown in Figure 9. Nevertheless, the energy stored/dissipated by the waffle-flat plate can be indirectly estimated as the difference between the energy stored/dissipated by the whole test structure, $W_{es} + W_p = E_I - W_k - W_\xi$, and the energy stored/dissipated by the columns $(W_{es} + W_p)_{columns}$ calculated in Section 4.4.1. The energy stored/dissipated by the plate calculated in this way is shown in Figure 13. Several aspects deserve attention. First, the energy stored/dissipated by the waffle-flat plate, $(W_{es} + W_p)_{plate}$, as well as the energy stored/dissipated by the columns is basically zero during tests B_5 and B_{32}, meaning the structure remained essentially elastic. This corroborates the response reported in Subsection 4.2.3 from the measurements of the strain gauges, the global force–displacement curves of Figures 7 and 8, and the observations. During test B_{190} and the following tests, the structure entered the nonlinear range and the amount of energy stored/dissipated by the plate $(W_{es} + W_p)_{plate}$ in relation to the total input energy E_I increased from $(W_{es} + W_p)_{plate}/E_I = 0.27$ for B_{190} to 0.63 for B_{682}, but interestingly, the percentage of energy

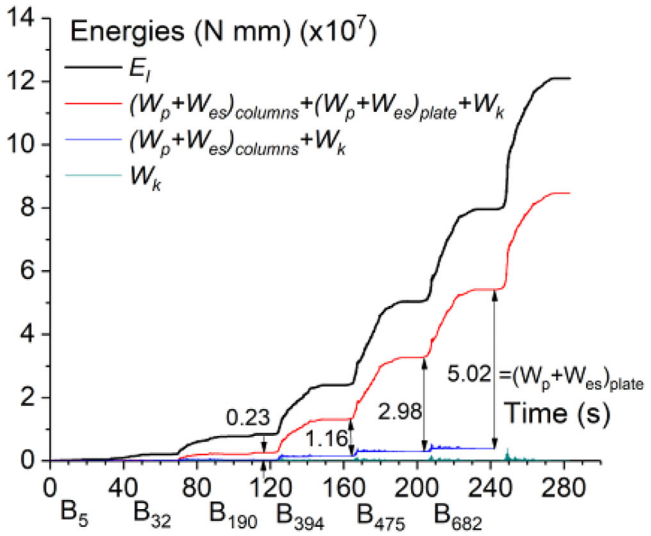

FIGURE 13 | Energy stored/dissipated by the waffle-flat plate.

stored/dissipated by the plate $(W_{es} + W_p)_{plate}$ in relation to the total amount of energy that contributes to damage E_D remained almost constant, ranging from $(W_{es} + W_p)_{plate}/E_D = 0.85$ for B_{190} to 0.93 for B_{682}. As for the relation between the energy stored/dissipated by the plate $(W_{es} + W_p)_{plate}$ in relation to that of the columns, $(W_{es} + W_p)_{columns}$, the ratio increased steadily from $(W_{es} + W_p)_{plate}/(W_{es} + W_p)_{columns} = 7$ for test B_{190} to $(W_{es} + W_p)_{plate}/(W_{es} + W_p)_{columns} = 12.9$ in test B_{682}. Most of the plastic strain energy dissipation of the plate occurred on the exterior plate–column connection.

4.5 | Chord Rotation at Column Ends

Figure 14 shows the chord rotations in the X and Y directions, θ_X, θ_Y, at each column end. They were determined as the ratio of the relative displacement of the top to the bottom column ends over the column height. The yield rotation θ_y of each hinge was calculated with the equations of 2G of Eurocode 8, part EN1998-1-1 [25], and is plotted in Figure 14 with bold blue dashed circles. The ultimate rotation θ_u of each hinge was also calculated with the equations of 2G of Eurocode 8, part EN1998-1-1 [25], and is plotted in Figure 14 with bold red dot-dash circles for tests B_{394} to B_{1218}. Also plotted for these tests are the rotations $\theta_{SD} = [\theta_y + 0.5(\theta_u - \theta_y)]/\gamma_{Rd,SD}$ (thin green dot circles) associated with the attainment of the LS of SD, and the

10969845, 0, Downloaded from https://onlinelibrary.wiley.com/doi/10.1002/eqe.70016 by Readcube (Labtiva Inc.), Wiley Online Library on [01/07/2025]. See the Terms and Conditions (https://onlinelibrary.wiley.com/terms-and-conditions) on Wiley Online Library for rules of use; OA articles are governed by the applicable Creative Commons License

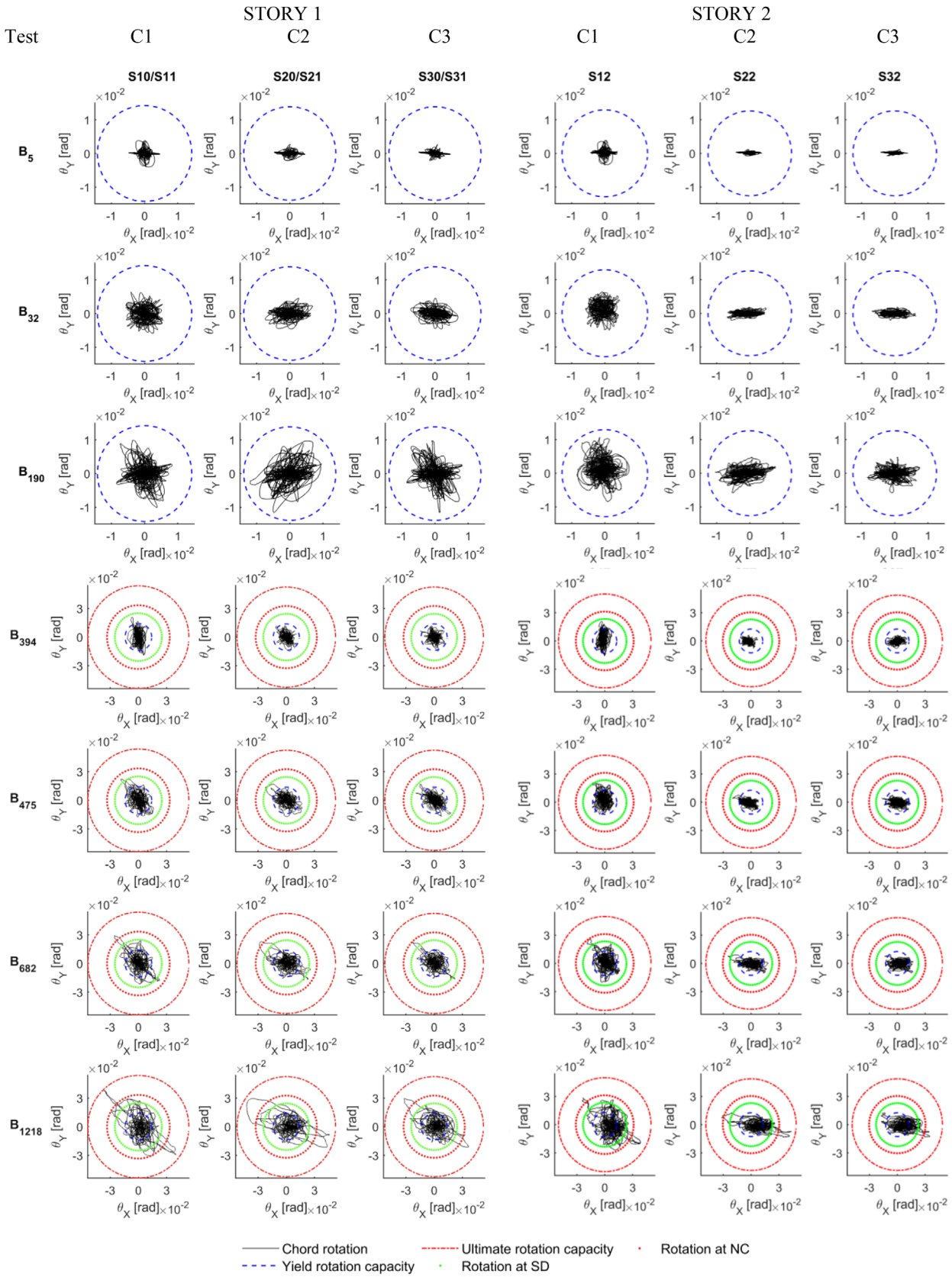

FIGURE 14 | Chord rotations in columns.

10969845, 0, Downloaded from https://onlinelibrary.wiley.com/doi/10.1002/eqe.70016 by Readcube (Labtiva Inc.), Wiley Online Library on [01/07/2025]. See the Terms and Conditions (https://onlinelibrary.wiley.com/terms-and-conditions) on Wiley Online Library for rules of use; OA articles are governed by the applicable Creative Commons License

TABLE 6 | Maximum chord rotations in columns normalized by the yield rotation.

Story	Column	B_5		B_{32}		B_{190}		B_{394}		B_{475}		B_{682}		B_{1218}	
		$\frac{\theta_{sqrt}}{\theta_y}$	$\frac{\theta_{mXY}}{\theta_y}$	$\frac{\theta_{sqrt}}{\theta_y}$	$\frac{\theta_{mXY}}{\theta_y}$	$\frac{\theta_{sqrt}}{\theta_y}$	$\frac{\theta_{mXY}}{\theta_y}$	$\frac{\theta_{sqrt}}{\theta_y}$	$\frac{\theta_{mXY}}{\theta_y}$	$\frac{\theta_{sqrt}}{\theta_y}$	$\frac{\theta_{mXY}}{\theta_y}$	$\frac{\theta_{sqrt}}{\theta_y}$	$\frac{\theta_{mXY}}{\theta_y}$	$\frac{\theta_{sqrt}}{\theta_y}$	$\frac{\theta_{mXY}}{\theta_y}$
2	C1	0.33	0.33	0.51	0.49	0.88	0.83	1.62	1.60	1.88	1.59	2.36	1.97	3.34	2.99
2	C2	0.34	0.34	0.55	0.54	0.83	0.83	0.97	0.93	1.63	1.60	2.05	1.97	3.51	3.46
2	C3	0.34	0.34	0.54	0.54	0.66	0.66	1.00	0.98	1.40	1.36	1.51	1.36	2.96	2.79
1	C1	0.34	0.34	0.54	0.45	0.81	0.71	1.54	1.47	2.03	1.57	2.73	2.07	3.70	2.82
1	C2	0.34	0.34	0.55	0.54	0.90	0.86	1.13	1.06	1.87	1.59	2.58	2.10	3.52	3.32
1	C3	0.36	0.36	0.54	0.53	0.84	0.83	1.17	1.07	1.62	1.41	2.38	1.71	3.15	2.63

TABLE 7 | Maximum chord rotations in columns normalized by the ultimate rotation.

Story	Column	B_5		B_{32}		B_{190}		B_{394}		B_{475}		B_{682}		B_{1218}	
		$\frac{\theta_{sqrt}}{\theta_u}$	$\frac{\theta_{mXY}}{\theta_u}$	$\frac{\theta_{sqrt}}{\theta_u}$	$\frac{\theta_{mXY}}{\theta_u}$	$\frac{\theta_{sqrt}}{\theta_u}$	$\frac{\theta_{mXY}}{\theta_u}$	$\frac{\theta_{sqrt}}{\theta_u}$	$\frac{\theta_{mXY}}{\theta_u}$	$\frac{\theta_{sqrt}}{\theta_u}$	$\frac{\theta_{mXY}}{\theta_u}$	$\frac{\theta_{sqrt}}{\theta_u}$	$\frac{\theta_{mXY}}{\theta_u}$	$\frac{\theta_{sqrt}}{\theta_u}$	$\frac{\theta_{mXY}}{\theta_u}$
2	C1	0.09	0.09	0.13	0.13	0.23	0.22	0.42	0.42	0.49	0.41	0.61	0.51	0.87	0.77
2	C2	0.09	0.09	0.14	0.14	0.22	0.22	0.25	0.24	0.42	0.41	0.53	0.51	0.91	0.90
2	C3	0.09	0.09	0.14	0.14	0.17	0.17	0.26	0.25	0.36	0.35	0.39	0.35	0.77	0.72
1	C1	0.09	0.09	0.14	0.12	0.21	0.19	0.41	0.39	0.54	0.42	0.72	0.55	0.98	0.74
1	C2	0.09	0.09	0.15	0.14	0.24	0.23	0.30	0.28	0.49	0.42	0.68	0.55	0.93	0.88
1	C3	0.09	0.09	0.14	0.14	0.22	0.22	0.31	0.28	0.43	0.37	0.63	0.45	0.83	0.70

TABLE 8 | Maximum chord rotations in columns normalized by the rotation at the LS SD.

Story	Column	B_5		B_{32}		B_{190}		B_{394}		B_{475}		B_{682}		B_{1218}	
		$\frac{\theta_{sqrt}}{\theta_{SD}}$	$\frac{\theta_{mXY}}{\theta_{SD}}$	$\frac{\theta_{sqrt}}{\theta_{SD}}$	$\frac{\theta_{mXY}}{\theta_{SD}}$	$\frac{\theta_{sqrt}}{\theta_{SD}}$	$\frac{\theta_{mXY}}{\theta_{SD}}$	$\frac{\theta_{sqrt}}{\theta_{SD}}$	$\frac{\theta_{mXY}}{\theta_{SD}}$	$\frac{\theta_{sqrt}}{\theta_{SD}}$	$\frac{\theta_{mXY}}{\theta_{SD}}$	$\frac{\theta_{sqrt}}{\theta_{SD}}$	$\frac{\theta_{mXY}}{\theta_{SD}}$	$\frac{\theta_{sqrt}}{\theta_{SD}}$	$\frac{\theta_{mXY}}{\theta_{SD}}$
2	C1	0.18	0.18	0.28	0.27	0.49	0.46	0.90	0.88	1.04	0.88	1.30	1.09	1.84	1.65
2	C2	0.19	0.19	0.30	0.30	0.46	0.46	0.53	0.51	0.90	0.88	1.13	1.09	1.94	1.91
2	C3	0.19	0.19	0.30	0.30	0.37	0.36	0.55	0.54	0.77	0.75	0.84	0.75	1.63	1.54
1	C1	0.19	0.19	0.30	0.26	0.46	0.40	0.87	0.83	1.15	0.89	1.55	1.18	2.10	1.60
1	C2	0.19	0.19	0.31	0.30	0.51	0.49	0.64	0.60	1.06	0.91	1.46	1.19	2.00	1.88
1	C3	0.20	0.20	0.30	0.30	0.48	0.47	0.67	0.61	0.92	0.80	1.35	0.97	1.79	1.49

rotation $\theta_{NC} = \theta_u / \gamma_{Rd,SD}$ associated with the attainment of the LS of NC (thin red dot circles), according to 2G of Eurocode 8 part EN1998-1-2 [2]. Tables 6 to 9 summarize the maximum rotations calculated in two different ways, $\theta_{sqrt} = \max\{(\theta_x^2 + \theta_y^2)^{1/2}\}$ and $\theta_{mXY} = \max\{\theta_x, \theta_y\}$, normalized by θ_y, θ_u, θ_{SD}, and θ_{NC}, respectively. During tests B_5 and B_{32}, the chord rotations remained below θ_y, and did not exceed approximately $0.5\theta_y$. During B_{190}, the rotations were below θ_y, yet very close, hence under this test the column ends remained basically elastic. During test B_{394} the chord rotations of all columns exceeded θ_y by up to two times and approached θ_{SD}. The incursion in the nonlinear range was, however, moderate. The response in terms of chord rotations during test B_{475} was similar to test B_{394} yet in this case all columns came very close to θ_{SD}; and at the base of column C1 it was slightly exceeded (15%) but still below θ_{NC}. Under test B_{682} the chord rotations exceeded θ_{SD} in most columns by up to 55% and got very close to θ_{NC}. During the last test B_{1218}, the chord rotations of all columns exceeded θ_{NC} by up to 58% and approached θ_u.

5 | Design Implications

5.1 | Behavior Factors for Applying the Reduced-Spectrum Force-Based Approach

The 2G of Eurocode 8 [2] allows the verification of WFP systems for the LS of SD using the force-based approach. This approach resorts to the behavior factor q that in the 2G of EN1998 part EN1998-1-1 [25] is the product of three components $q = q_R q_S q_D$. Here, q_R accounts for the overstrength because of a redistribution of seismic action in redundant structures, q_S accounts for

10969845, 0, Downloaded from https://onlinelibrary.wiley.com/doi/10.1002/eqe.70016 by Readcube (Labtiva Inc.), Wiley Online Library on [01/07/2025]. See the Terms and Conditions (https://onlinelibrary.wiley.com/terms-and-conditions) on Wiley Online Library for rules of use; OA articles are governed by the applicable Creative Commons License

TABLE 9 | Maximum chord rotations in columns normalized by the rotation at the LS NC.

Story	Column	B_5		B_{32}		B_{190}		B_{394}		B_{475}		B_{682}		B_{1218}	
		$\frac{\theta_{sqrt}}{\theta_{NC}}$	$\frac{\theta_{mXY}}{\theta_{NC}}$	$\frac{\theta_{sqrt}}{\theta_{NC}}$	$\frac{\theta_{mXY}}{\theta_{NC}}$	$\frac{\theta_{sqrt}}{\theta_{NC}}$	$\frac{\theta_{mXY}}{\theta_{NC}}$	$\frac{\theta_{sqrt}}{\theta_{NC}}$	$\frac{\theta_{mXY}}{\theta_{NC}}$	$\frac{\theta_{sqrt}}{\theta_{NC}}$	$\frac{\theta_{mXY}}{\theta_{NC}}$	$\frac{\theta_{sqrt}}{\theta_{NC}}$	$\frac{\theta_{mXY}}{\theta_{NC}}$	$\frac{\theta_{sqrt}}{\theta_{NC_{SD}}}$	$\frac{\theta_{mXY}}{\theta_{NC}}$
2	C1	0.14	0.14	0.21	0.20	0.37	0.35	0.67	0.66	0.78	0.66	0.98	0.82	1.39	1.24
2	C2	0.14	0.14	0.23	0.23	0.34	0.34	0.40	0.38	0.68	0.66	0.85	0.82	1.46	1.44
2	C3	0.14	0.14	0.22	0.22	0.28	0.27	0.42	0.41	0.58	0.56	0.63	0.56	1.23	1.16
1	C1	0.14	0.14	0.23	0.19	0.35	0.30	0.66	0.62	0.86	0.67	1.16	0.88	1.57	1.20
1	C2	0.15	0.15	0.23	0.23	0.38	0.37	0.48	0.45	0.80	0.68	1.10	0.89	1.50	1.41
1	C3	0.15	0.15	0.23	0.22	0.36	0.35	0.50	0.46	0.69	0.60	1.01	0.73	1.34	1.12

overstrength due to all other sources, and q_D accounts for the plastic deformation capacity. 2G of Eurocode 8 establishes that for all types of structures $q_S \leq 1.5$, and for torsional flexible structures $q_R = 1$. The product $q_R q_S$ represents the ratio between the base shear force at yielding and the design base shear force, which can be expressed as the ratio between the base shear force coefficients α_B and α_{design} calculated in Sections 4.2.1 and 2.1. Using the values of α_{design} and α_B obtained in the tests gives $\alpha_{BX}{}^{+}/\alpha_{design} = 0.37/0.33 = 1.12$ and $\alpha_{BX}{}^{-}/\alpha_{design} = 0.33/0.33 = 1.0$ for the positive and negative X direction, and $\alpha_{BY}{}^{+}/\alpha_{design} = 0.30/0.33 = 0.91$ and $\alpha_{BY}{}^{-}/\alpha_{design} = 0.40/0.33 = 1.21$ for the positive and negative Y direction. The respective mean values are $\alpha_{BX}/\alpha_{design} = 1.06$ and $\alpha_{BY}/\alpha_{design} = 1.06$ for the X and Y directions. These values are about 30% smaller than the maximum $q_R q_S = 1.1{\cdot}1.5 = 1.65$ established by 2G of EN1998 for WFP systems, reduced in the case of torsional flexible structures to $q_R q_S = 1.0{\cdot}1.5 = 1.50$. In turn, the ductility factors μ obtained from the capacity curve when the specimen reaches the LS of NC reported in Section 4.2.1 are $\mu_X{}^{+} = 3.7$, $\mu_X{}^{-} = 5.1$ in the positive and negative X direction, and $\mu_Y{}^{+} = 3.4$, $\mu_Y{}^{-} = 3.3$ in the positive and negative Y direction; the mean values are $\mu_X = 4.4$ and $\mu_Y = 3.4$. The plastic deformation of the tested specimen associated with the LS of SD along the X and Y directions, $\mu_{X,SD}(= \delta_{TX,SD}/\delta_{TX,y})$, and $\mu_{Y,SD}(= \delta_{TY,SD}/\delta_{TY,y})$, can be estimated from the ductility factors $\mu_X(= \delta_{TX}/\delta_{TX,y})$ and $\mu_Y(= \delta_{TY}/\delta_{TY,y})$ associated with the LS of NC by applying the same rationale used by 2G of EN1998 [2] to define the chord rotation θ_{SD} from θ_y and θ_u, i.e., $\theta_{SD} = [\theta_y + 0.5(\theta_u - \theta_y)]\ /\gamma_{Rd,SD}$ or $\theta_{SD}/\ \theta_y = [1 + 0.5(\theta_u/\theta_y - 1)]\ /\gamma_{Rd,SD}$. Here, $\gamma_{Rd,SD}$ is a partial safety factor of the 2G of Eurocode 8. This gives $\delta_{TX,SD}/\ \delta_{TX,y} = 0.5[1 + (\delta_{TX}/\delta_{TX,y})]/\gamma_{Rd,SD}$ or $\mu_{X,SD} = 0.5[1 + \mu_X]/\gamma_{Rd,SD}$ in the X direction, and $\mu_{Y,SD} = 0.5[1 + \mu_Y]/\gamma_{Rd,SD}$ in the Y direction. Specializing these expressions for $\mu_X = 4.4$ and $\mu_Y = 3.4$ and adopting the value of $\gamma_{Rd,SD}(= 1.35)$ recommended by 2G of Eurocode 8 [2] gives $\mu_{X,SD} = 2.\ 0$ and $\mu_{Y,SD} = 1.6$. The value of the factor q_D prescribed by 2G of EN1998 [2] for WFP systems is 1.2, that is, close to $\min\{\mu_{X,SD}, \mu_{Y,SD}\} = 1.6$ and slightly below the mean obtained from the tests $(\mu_{X,SD} + \mu_{Y,SD})/2 = 1.8$. The behavior factor q $(= q_R q_S q_D)$ prescribed by 2G of EN1998 [2] for WFP systems is $q = 2$ for nontorsional flexible structures, and $q = 2{\cdot}0.8 = 1.6$ for torsional flexible structures. The counterpart quantities obtained from the tests are $(\alpha_{BX}/\alpha_{design})\mu_{X,SD} = 1.06{\cdot}2.0 = 2.12$ and $(\alpha_{BY}/\alpha_{design})\mu_{Y,SD} = 1.06{\cdot}1.6 = 1.70$. Taking into account that the tested specimen is torsional flexible according to the criteria established by 2G of Eurocode 8 [2], the minimum total behavior factor obtained in the tests (1.7) is slightly above the one (1.6) prescribed by 2G of Eurocode 8 [2].

5.2 | Design of the Exterior Plate–Column Connection

Most of the plastic strain energy was dissipated by the plate at the exterior plate–column connection where damage concentrated. This emphasizes the importance of having transverse beams properly reinforced for torsion in the perimeter of the plate and punching shear reinforcement. Attention should also be paid to putting longitudinal reinforcement crossing the plate–column interface so that, through a dowel action, the plate can hang from the column when the structure attains the ultimate limit state.

6 | Conclusions

A two-fifth scale portion of an RC waffle-flat plate structure designed according to current codes was tested under bidirectional horizontal seismic loadings on a shake table that reproduced near-fault ground motions. The specimen was subjected to seven tests of increasing intensity, representing very frequent, frequent, design, and maximum considered rare earthquakes at the assumed building site (Granada, Spain) for a building of consequence class CC2 (residential) according to 2G of Eurocode 8. Given the results of the tests, the following conclusions are put forth:

1. The structure responded basically as expected in design. Under very frequent earthquakes with return periods up to 32 years, the structure remained perfectly elastic and without damage. Under a frequent earthquake with a return period of 190 years, the structure responded essentially within the elastic range and it was only slightly damaged. Under two consecutive severe earthquakes with return periods of 394 and 475 years, representing approximately the design basis earthquake, the structure entered the nonlinear range and suffered SD at column ends—where maximum chord rotations came very close to the limit established by the 2G of Eurocode 8—and at the plate in the exterior plate–column connection. Under a rare earthquake having a return period of 682 years, the structure was on the brim of collapse. The structure collapsed under a rare earthquake whose return period, 1218 years, was below the 1600 years that the 2G of Eurocode 8 associates with the LS of NC. Despite this, the performance of the structure is deemed satisfactory, as in the last test the specimen had accumulated the damage of previous testing.

10969845, 0, Downloaded from https://onlinelibrary.wiley.com/doi/10.1002/eqe.70016 by Readcube (Labtiva Inc.), Wiley Online Library on [01/07/2025]. See the Terms and Conditions (https://onlinelibrary.wiley.com/terms-and-conditions) on Wiley Online Library for rules of use; OA articles are governed by the applicable Creative Commons License

2. The type of plastic mechanism developed by the plate–column connections when the structure reached the LS of SD was of the strong plate-weak column type for the interior connections, and weak plate-strong column mechanism for the exterior connection.

3. Damage concentrated at the exterior plate–column connection and at the base of the columns. The transverse (edge) beams of the plate failed in torsion in the vicinity of the exterior column, and this triggered the loss of the moment transfer capacity of the exterior plate–column connection. The dowel action of the longitudinal reinforcement crossing the plate–column interface prevented the plate from falling.

4. The total (accumulated) energy input by the two components of the near-fault ground motion to the structure when it collapsed (4.44 m/s in terms of equivalent velocity) is close to the value obtained on a similar specimen subjected to shake table tests with two components of a far-field ground motion (3.82 m/s) and also with one single component of a far-field earthquake (3.95 m/s). This means that the ultimate energy dissipation capacity of the specimen under near-fault or under far-field ground motion, or under a single or under two horizontal components of the ground motions, is basically the same.

5. The energy dissipated by the inherent damping of the structure, W_ξ, was estimated numerically assuming a mass-proportional damping matrix, and it was found to be consistent with the amount of total input energy, E_I, and the vibrational energy, W_e, evaluated experimentally from instrumentation in the low intensity tests B_5 and B_{35}, for which the structure remained basically elastic, and only E_I, W_ξ and W_e are involved in the energy balance equation of the structure. This estimation was also performed for the test involving large plastic deformations; it was found that the portion of E_I dissipated by inherent damping, $W_{\xi,}$ decreases as the structure undergoes larger plastic deformations, representing only 30% of E_I at the end of the tests, while most of the other 70% resulted in damage to the structure.

6. Most of the energy contributing to damage E_D $(= E_I - W_\xi)$ as defined by Housner was basically stored/dissipated by the plate at the exterior plate–column connection. The percentage of the energy stored/dissipated by the plate $(W_{es} + W_p)_{plate}$ in relation to E_I increased from 27% to 63% as the severity of the ground motion increased, but the percentage of $(W_{es} + W_p)_{plate}$ in relation to E_D remained almost constant, ranging from 85% to 93%.

7. The energy stored/dissipated by the plate $(W_{es} + W_p)_{plate}$ in relation to that of the columns, $(W_{es} + W_p)_{columns}$, increased steadily from $(W_{es} + W_p)_{plate}/(W_{es} + W_p)_{columns} = 7$ for the low levels of seismic action to $(W_{es} + W_p)_{plate}/(W_{es} + W_p)_{columns} = 12.9$ for high levels of the ground motion. The amount of energy dissipated by the columns when the structure approached collapse was very small (less than 7%) in comparison with that dissipated by the plate at the exterior plate–column connection. This emphasizes the importance of paying attention to the design of the plate at the exterior plate–column connections.

8. The capacity curve of the tested structure was estimated from the experimental base shear vs. top displacement relationship as an envelope of the points with zero velocity. The behavior factor of the structure was determined from this curve, giving a value (1.55) that is very close to the behavior factor ($q = 1.6$) prescribed by the 2G of Eurocode 8 for torsionally flexible flat-plate systems for use with force-based seismic design methods.

Acknowledgements

This work was supported by the Spanish Ministry of Science MCIN/AEI/10.13039/501100011033/[PID2023-152739OB-I00]; and FEDER (Fonds Européen de Dévelopment Régional).

Conflicts of Interest

The authors declare no conflicts of interest.

Data Availability Statement

The data that support the findings of this study are available from the corresponding author upon reasonable request.

References

1. CEN, *Eurocode 8: Design of Structures for Earthquake Resistance, Part 1: General Rules, Seismic Actions and Rules for Buildings. European Standard EN 1998-1:2004* European Committee for Standardization (2004).

2. CEN, *Eurocode 8: Design of Structures for Earthquake Resistance Part 1–2: Buildings; prEN1998-1-2:2024* (European Committee for Standardization, 2024).

3. Ministerio Fomento, *Norma de Construcción Sismorresistente. Parte General y Edificación (NCSE-02)* (Centro Publicaciones, 2003).

4. I. Robertson and G. Johnson, "Cyclic Lateral Loading of Nonductile Slab–Column Connections," *ACI Structural Journal* 103 (2006): 356–364.

5. I. S. Drakatos, A. Muttoni, and K. Beyer, "Internal Slab-Column Connections Under Monotonic and Cyclic Imposed Rotations," *Engineering Structures* 123 (2016): 501–516.

6. Y. Zhou and M. B. D. Hueste, *Review of Test Data for Interior Slab-Column Connections With Moment Transfer*, Vol. 315 (ACI Special Publication, 2017), 141–166.

7. A. Ramos, R. Marreiros, A. Almeida, B. Isufi, and M. Inacio, *Punching of Flat Slabs Under Reversed Horizontal Cyclic Loading*, Vol. 315 (ACI Special Publication, 2017), 253–272.

8. C. Rha, T. H.-K. Kang, M. Shin, and J. B. Yoon, "Gravity and Lateral Load-Carrying Capacities of Reinforced Concrete Flat Plate Systems," *ACI Structural Journal* 111, no. 4 (2014): 753–764.

9. D. R. Fick, M. A. Sozen, and M. E. Kreger, "Response of Full-Scale Three-Story Flat-Plate Test Structure to Cycles of Increasing Lateral Load," *ACI Structural Journal* 114, no. 6 (2017): 1507–1517.

10. D. Coronelli, M. L. Tornaghi, L. Martinelli, et al., "Testing of a Full-Scale Flat Slab Building for Gravity and Lateral Loads," *Engineering Structures* 243 (2021): 112551.

11. T. H. K. Kang and W. Wallace, "Shake Table Test of Reinforced Concrete Flat Plate Frames and Post-Tensioned Flat Plate Frames," in Proceedings of the 13 World Conference on Earthquake Engineering, Vancouver, Canada, 2004.

12. A. Benavent-Climent, J. Donaire-Avila, and E. Oliver-Saiz, "Shaking Table Tests of a Reinforced Concrete Waffle–Flat Plate Structure Designed Following Modern Codes: Seismic Performance and Damage Evaluation," *Earthquake Engineering and Structural Dynamics* 45 (2016): 315–336.

13. A. Benavent-Climent, D. Galé-Lamuela, and J. Donaire-Ávila, "Energy Capacity and Seismic Performance of RC Waffle-Flat Plate Structures

10969845, 0, Downloaded from https://onlinelibrary.wiley.com/doi/10.1002/eqe.70016 by Readcube (Labtiva Inc.), Wiley Online Library on [01/07/2025]. See the Terms and Conditions (https://onlinelibrary.wiley.com/terms-and-conditions) on Wiley Online Library for rules of use; OA articles are governed by the applicable Creative Commons License

Under Two Components of Far-Field Ground Motions: Shake Table Tests," *Earthquake Engineering and Structural Dynamics* 48 (2019): 949–969.

14. D. Coronelli, A. Muttoni, I. R. Pascu, A. Pinho Ramos, and T. Netti, "A State of the Art of Flat-Slab Frame Tests for Gravity and Lateral Loading," *Structural Concrete* 21, no. 6 (2020): 2764–2781.

15. N. M. Fardis, *Seismic Design, Assessment, and Retrofitting of Concrete Buildings Based on EN-Eurocode 8* (Springer, 2009).

16. B. Alavi and H. Krawinkler, "Behavior of Moment-resisting Frame Structures Subjected to Near-Fault Ground Motions," *Earthquake Engineering & Structural Dynamics* 33 (2004): 687–706.

17. E. Kalkan and S. K. Kunnath, "Effective Cyclic Energy as a Measure of Seismic Demand," *Journal of Earthquake Engineering* 11 (2007): 725–751.

18. E. Liossatou and M. N. Fardis, "Residual Displacements of RC Structures as SDOF Systems," *Earthquake Engineering and Structural Dynamics* 44, no. 4 (2015): 713–734.

19. Ministerio Fomento, *Instrucción de Hormigón Estructural. EHE-08* (2008).

20. Structural Engineers Association of California (SEAOC) & Vision 2000 Committee, *Vision 2000: Performance Based Seismic Engineering of Buildings*, Vol. 1 (1995).

21. H. Akiyama, *Earthquake-Resistant Limit-State Design for Buildings* (Tokyo, Japan: University of Tokyo Press, 1985).

22. G. W. Housner, "Limit Design of Structures to Resist Earthquakes," in Proceedings of the First World Conference on Earthquake Engineering (International Association for Earthquake Engineering [IAEE], 1956).

23. H. Park and T. Eom, "A Simplified Method for Estimating the Amount of Energy Dissipated by Flexure-Dominated Reinforced Concrete Members for Moderate Cyclic Deformations," *Earthquake Spectra* 22, no. 2 (2006): 459–490.

24. K. Maekawa, A. Pimanmas, and H. Okamura, *Non Linear Mechanics of Reinforced Concrete* (Spon Press, 2003).

25. CEN, *Eurocode 8: Design of Structures for Earthquake Resistance Part 1-1: General Rules and Seismic Action; prEN1998-1-1:2024* (European Committee for Standardization, 2024).

10969845, 0, Downloaded from https://onlinelibrary.wiley.com/doi/10.1002/eqe.70016 by Readcube (Labtiva Inc.), Wiley Online Library on [01/07/2025]. See the Terms and Conditions (https://onlinelibrary.wiley.com/terms-and-conditions) on Wiley Online Library for rules of use; OA articles are governed by the applicable Creative Commons License